UNIVERSITY OF COPENHAGEN
FACULTY OF SCIENCE

Master Thesis

Mia-Louise Nielsen

Transient Neutrino Astrophysics with IceCube-DeepCore

Supervisors: Dr. D. Jason Koskinen and Dr. Morten A. Medici

September 3, 2019

Abstract

Numerous types of astrophysical objects are visible in either electromagnetic radiation or gravitational waves and in some cases these messenger particles/waves may be accompanied by neutrinos. In multimessenger astronomy more than one messenger (photons, gravitational waves, neutrinos, and cosmic rays) are observed from a common origin with the potential to provide information about the sources.

In this work, the focus will be on neutrinos observed by the IceCube Neutrino Observatory.

An analysis is developed with the objective of finding low-energy (sub-TeV) neutrinos possibly originating from transient point sources with neutrino emission time scales of $\sim$600 seconds. The analysis is performed on three years of data from the GRECO data sample, which is the largest existing low-energy sample from the IceCube Neutrino Observatory.

The method used in the analysis consists of two parts, first a kernel density estimation is used to find multiplets of neutrinos in time, subsequently a maximum likelihood method is used to test for spatial clustering within the multiplets.

In the three years of IceCube data, no evidence of transient neutrino emission is found. Constraints are placed on the volumetric rate of transient point sources in the local universe.

Acknowledgment

I have really appreciated and enjoyed the last year that I have spent working on the IceCube project with the group at NBI. It has been very educational and I have learned a lot about both neutrino and astrophysics, as well as to enjoy statistics and coding. I want to thank Jason for giving me this opportunity and for supporting me all the way. I highly value how you have always shown trust in me and that you have pushed me to learn more, for example by continuously presenting my progress and results on the calls.

A special Thanks to Morten, with whom I have not only shared an office, but also countless discussions about physics as well as a never ending supply of sweets and chocolate cookies. You have always been very patient with me, even when I have asked the same question multiple times. Without you, my project would have been a lot harder and less enjoyable.

I would like to thank the whole IceCube group at NBI, especially Tom and Étienne, for always taking the time explain physics and help out with files, etc., whenever necessary.

I owe another thanks to Rameez for helping me with the files for the analysis and for helping me write the paper.

I appreciate that Markus has always been willing to discuss the astrophysics in my project with great patience. I have always found our discussions very interesting and informative.

I am truly happy that my family, my parents and my brother Mikkel, have always shown interest in and supported me throughout my education. It has been a delight to talk to you all about how my studies were going.

Author's contribution

I became a member of the IceCube collaboration around the middle of 2018 in order to help develop and perform a search for low-energy astrophysical point sources. The work has been done in collaboration with other IceCube members, e.g., Mohamed Rameez, and therefore my contributions will be specified here.

Specifically, the spatial part of the analysis described in Section 5.3 was developed, tested and, implemented by me. The angular resolution spline was originally created by Mohamed Rameez and combined tracks and cascades. I improved the spline by separating tracks and cascades and by refining the binning.

I have written the software able to estimate the sensitivity and discovery potential for the analysis and used this to study the impact on the performance by several parameters, e.g., the bandwidth of the KDE and the thresholds in the analysis. These results are shown in Section 5.4.2 and 5.5.

Further, the accuracy of the analysis's spatial part have been examined by me, and is presented in Section 5.4.1.

This resulted in the analysis being approved on July 11. Thereafter, I performed the analysis on three years of IceCube data and placed upper bounds on the rate per unit volume for transient point sources given the specific model under consideration. These results are presented in Chapter 6.

Furthermore, I am currently contributing to the process of writing the scientific paper that will be published presenting the results of the analysis. This includes having the paper outline approved by the collaboration on August 22, 2019.

Contents

List of Figures

List of Tables

Chapter 1

Introduction

Multimessenger astronomy is becoming an increasingly prominent area of research. With the detection of neutrinos from extragalactic astrophysical sources and the recent discovery of gravitational waves, astrophysical objects are no longer exclusively observed through electromagnetic radiation. Neutrinos are an excellent messenger due to their ability to travel in straight lines between their source and the Earth without being deflected by magnetic fields or interacting with matter. Therefore they can provide exciting information about even some of the densest regions in the universe.

The neutrino's very low interaction probability makes it capable of traveling large distances without interaction, however this property also makes the detection very difficult.

The IceCube Neutrino Observatory (IceCube) is a large scale particle detector located in the glacial ice at the South Pole. Due to the size of the detector and the neutrino being the second most abundant particle in the universe, numerous neutrinos are detected by IceCube every year. These neutrinos will have various different origins, atmospheric as well as astrophysical.

Multiple analyses aiming to show correlations between astrophysical sources and high energy neutrinos have been performed within the IceCube Collaboration. However, searches/studies of astrophysical phenomena emitting neutrinos in the low-energy range (sub-TeV) are few and a correlation between such neutrinos and confirmed astrophysical sources has yet to be found.

The objective of this work is to develop a method able to observe transient astrophysical point sources in the data from IceCube. In principle, the analysis should function both as an offline analysis on already existing archived data as well as an online real-time search/alert system. The purpose of the real-time search is to produce alerts of interest for experiments observing transient point sources through other messengers, e.g., the Fermi Gamma-ray Space Telescope. In this work, the analysis is developed and applied to archived data, while the

implementation of the online alert system will take place in the future.

Chapter 2 introduces neutrinos within the Standard Model and beyond. The physics of the IceCube detector together with the detection of neutrinos including neutrino interactions, Cherenkov radiation, and event topologies will be described in Chapter 3. Chapter 4 provides the theoretical framework of the astrophysics relevant for the analysis, i.e., a description of possible astrophysical sources, specifically gamma-ray bursts and the mechanism behind their emission of neutrinos. The atmospheric background is discussed as well. The analysis is described in detail in Chapter 5, followed by the results in Chapter 6. Finally, in Chapter 7, the concluding remarks and future prospects will be presented.

Chapter 2

Neutrinos — in the Standard Model and beyond

The neutrino is an elementary particle that will be the center of attention in this work. It is partly described by the Standard Model, however, additional physics beyond the Standard Model is necessary in order to fully understand and describe the properties of the neutrino.

A discussion of the neutrino in the context of the Standard Model is given in Section 2.1, while neutrino oscillation (the physics beyond the Standard Model), is described briefly in Section 2.2.

2.1 Neutrinos in the Standard Model

Without the existence of the neutrino, the energy of the emitted electron from a beta-decay would be expected to equal a single specific value every time, in accordance with a general two-body decay. However, the energy of the emitted electron has been measured to be distributed over a range of energies, which in 1930 led to the prediction of the neutrino [1]. The existence of neutrinos was confirmed in the 1950s in the *Cowan-Reines neutrino experiment*, where antielectron neutrinos were detected after being created in a nuclear reactor [2].

Neutrinos are elementary particles representing the neutral leptons in the Standard Model. They are paired together with an electrically charged and more massive lepton in doublets, see Figure 2.1. They exist in three different *flavors* associated with the other lepton in the doublet.

Since neutrinos have no electric charge, they do not couple to the photon, the carrier of the electromagnetic force. Therefore, neutrinos do not interact electromagnetically. Furthermore, neutrinos are *colorless*, meaning that they cannot interact via the strong force by coupling to gluons. In the framework

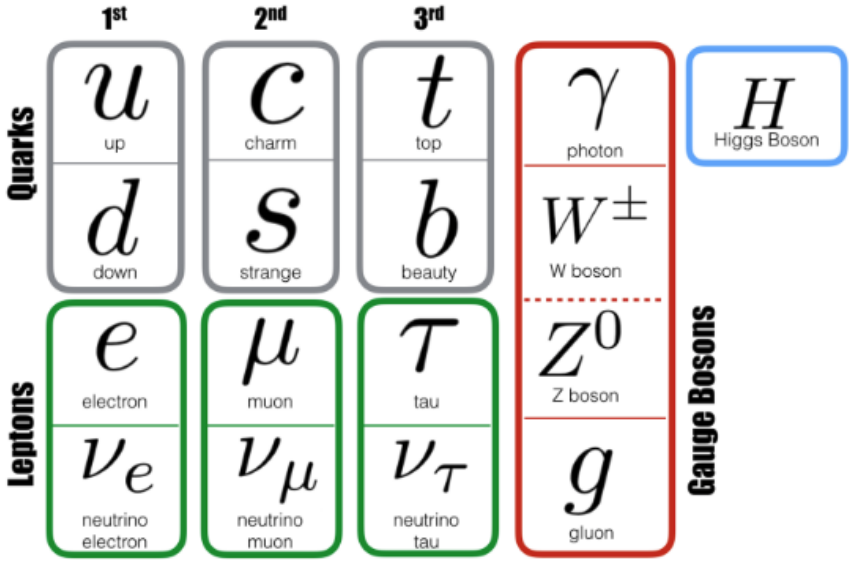

FIGURE 2.1: *Illustrative chart of the particles in the Standard Model containing the six quarks, the three charged leptons, three neutral leptons (neutrinos), four gauge bosons and the Higgs boson. From [3].*

of the Standard Model, neutrinos only interact weakly through the exchange of the $W^{\pm}$ and Z^0 bosons with a very small interaction probability.

As a result of their small cross section and because they do not interact electromagnetically, neutrinos are excellent messenger particles for astrophysical phenomena. However, these properties are also the reason for the difficulties of the neutrino detection. This will be discussed in later chapters.

In the Standard Model, neutrinos do not interact with the Higgs boson and are therefore predicted to be massless. However, it has been shown that neutrinos actually are massive, and consequently, they interact gravitationally in addition to weakly.

2.2 Flavor oscillation

Neutrinos exist in three flavors, which in the Standard Model are predicted to be massless.

In the 1960s an experiment was performed in a mine in South Dakota with the purpose of measuring the solar neutrino flux [4, 5]. The neutrino flux originating from the Sun was described by the Standard Solar Model, where electron neutrinos are emitted from the Sun after being produced in hydrogen fusion

processes and beta-decays, e.g.

$$\mathrm{p} + \mathrm{p} \rightarrow \mathrm{D} + \mathrm{e}^{+} + \nu_e, \qquad {}^{8}_{5}\mathrm{B} \rightarrow {}^{8}_{4}\mathrm{Be}^{\star} + \mathrm{e}^{+} + \nu_e.$$

With more than 600 tons of chlorine-based fluid, the aim was for the neutrinos to interact with the fluid via the inverse beta-decay

$$\nu_e + {}^{37}_{17}\mathrm{Cl} \rightarrow {}^{37}_{18}\mathrm{Ar} + \mathrm{e}^{-}.$$

Subsequently, the number of argon atoms could be counted due to their radioactive properties. The observed rate was only approximately one third of the predicted rate from the Solar Standard Model. This was known as the *solar neutrino problem*. This was an indication that either something was wrong with the experiment, or the understanding of the neutrino emission from the Sun, or new physics beyond the Standard Model was necessary in order to fully understand and explain the behavior of the neutrinos.

Throughout the next few decades other experiments followed up on the results including Sudbury Neutrino Observatory (SNO) [6]. This experiment was able to measure both the electron neutrino flux as well as the total neutrino flux and thereby estimate the fraction of electron neutrinos from the Sun. Their results indicated that the missing electron neutrinos had undergone a change of flavor during their travel towards the Earth.

The solar neutrino problem was solved by introducing the theory of the oscillation between the flavors, leading to a better understanding of the properties of the neutrinos.

Neutrinos interact via their flavor states (ν_e, ν_μ, ν_τ) but propagate through space as their mass eigenstates (ν_1, ν_2, ν_3), and neutrino oscillation occurs because the mass states are different from the flavor states. The flavor states are related to the mass states through the 3×3 *PMNS (Pontecorvo-Maki-Nakagawa-Sakata)* matrix [7, 8] (see Appendix A for a derivation of transition probabilities given a two-flavor model)

$$\begin{bmatrix} \nu_e \\ \nu_\mu \\ \nu_\tau \end{bmatrix} = \begin{bmatrix} U_{e1} & U_{e2} & U_{e3} \\ U_{\mu1} & U_{\mu2} & U_{\mu3} \\ U_{\tau1} & U_{\tau2} & U_{\tau3} \end{bmatrix} \begin{bmatrix} \nu_1 \\ \nu_2 \\ \nu_3 \end{bmatrix}. \tag{2.1}$$

This is a unitary matrix describing the mixing between the states, i.e., neutrinos propagate through space as their mass states that are superpositions of the flavor states. In order to parameterize the matrix, three mixing angles (θ_{12}, θ_{23}, and θ_{13}) are needed together with a complex phase factor δ_{CP}. The mixing angles describe the rotation between the flavor states relative to the mass states,

while the phase factor is related to the *charge-parity violation*. In terms of these four parameters Equation 2.1 can be written as [7, 8]

$$\begin{aligned}\begin{bmatrix}\nu_e\\ \nu_\mu\\ \nu_\tau\end{bmatrix} &= \begin{bmatrix}1 & 0 & 0\\ 0 & c_{23} & s_{23}\\ 0 & -s_{23} & c_{23}\end{bmatrix}\begin{bmatrix}c_{13} & 0 & s_{13}e^{-i\delta_{CP}}\\ 0 & 1 & 0\\ -s_{13}e^{i\delta_{CP}} & 0 & c_{13}\end{bmatrix}\begin{bmatrix}c_{12} & s_{12} & 0\\ -s_{12} & c_{12} & 0\\ 0 & 0 & 1\end{bmatrix}\begin{bmatrix}\nu_1\\ \nu_2\\ \nu_3\end{bmatrix},\\ &= \begin{bmatrix}c_{12}c_{13} & s_{12}c_{13} & s_{13}e^{-i\delta_{CP}}\\ -s_{12}c_{23} - c_{12}s_{23}s_{13}e^{i\delta_{CP}} & c_{12}c_{23} - s_{12}s_{23}s_{13}e^{i\delta_{CP}} & s_{23}c_{13}\\ s_{12}s_{23} - c_{12}c_{23}s_{13}e^{i\delta_{CP}} & -c_{12}s_{23} - s_{12}c_{23}s_{13}e^{i\delta_{CP}} & c_{23}c_{13}\end{bmatrix}\begin{bmatrix}\nu_1\\ \nu_2\\ \nu_3\end{bmatrix}.\end{aligned} \tag{2.2}$$

The shortened notation $s_{ij} = \sin(\theta_{ij})$ and $c_{ij} = \cos(\theta_{ij})$ has been adopted. The three mixing angles are determined experimentally. Experiments measuring solar neutrinos are especially sensitive to θ_{12}, and for that reason, this angle is often dubbed the *solar mixing angle* $\theta_\odot$. It has been measured to $\theta_{12} \sim 34°$. The largest mixing angle is $\theta_{23} \sim 45°$, which corresponds to approximately maximal mixing. In 2012 it was confirmed that the last angle is non-zero, $\theta_{13} \sim 9°$ [9].

Neutrinos produced by an astrophysical source with a specific initial flavor ratio will oscillate during their travel toward the Earth and therefore arrive with a different final flavor ratio. This impacts the searched for astrophysical transients, and will be discussed in more detail in Sections 4.2 and 5.1.2.

Chapter 3

IceCube Neutrino Observatory and detection of neutrinos

The IceCube Neutrino Observatory is a large scale detector consisting of 1 cubic kilometer of instrumented ice located at the South Pole.

This chapter provides a general description of the detector as well as the interactions of neutrinos. This is followed by a discussion of the production of Cherenkov radiation and the different event topologies, and finally, detector noise will be explained

3.1 The IceCube detector

The IceCube Neutrino Observatory (IceCube), is a large detector consisting of instrumented ice. It contains 86 *strings* each composed of 60 digital optical modules (DOMs). These DOMs are located 1450 – 2450 meters under the surface. In total, the strings are embedded within approximately one cubic kilometer of ice, with a surface at the top of about 1 square kilometer. The strings are mostly distributed in a hexagonal shape. An illustration of the detector is shown in Figure 3.1.

The main part of the detector, the In-Ice array, contains the 86 strings and is located deep below the surface of the ice. The In-Ice array aims to detect neutrinos of astrophysical origin with energies ranging from $\mathcal{O}$(TeV) to $\mathcal{O}$(PeV).

Additionally, 324 optical sensors are placed at the surface in the IceTop, with the purpose of observing cosmic ray showers.

In the center of the In-Ice array, the sub-array DeepCore is located. This is a denser instrumented part of IceCube consisting of a subset of 8 strings of the In-Ice array. The objective of DeepCore is to increase the sensitivity at lower energies and thereby allow the observation of neutrinos down to $\sim$10 GeV [10].

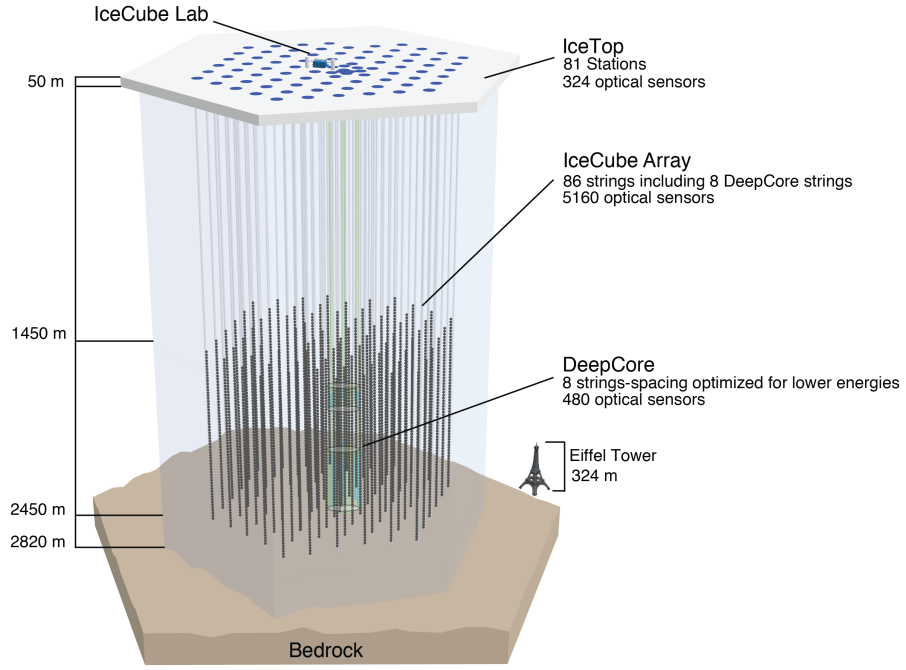

FIGURE 3.1: *Illustration of the IceCube Neutrino Observatory with the IceTop on the top of the ice, the In-Ice array buried deeply in the glacial ice, and the DeepCore located in the center of the In-Ice array. Modified from [11].*

3.1.1 Digital optical modules

Each string contains 60 DOMs, which are the units in IceCube that are acquiring data by measuring the light emitted when neutrinos interact in the ice — this will be discussed in greater detail in the next section. Each DOM consists of a glass shell protecting the interior, see Figure 3.2. Inside, the ∼10-inch photomultiplier tube (PMT) is located pointing downwards (to the north). The PMTs are capable of detecting single photons with wavelengths ranging from 300 nm to 650 nm, i.e., they are effective in the ultraviolet and visible parts of the electromagnetic spectrum. This is a result of the high quantum efficiencies of approximately 25% for the standard PMTs. The strings represented in DeepCore have a quantum efficiency that is up to 35% higher compared to the standard PMTs, leading to an increased sensitivity of DeepCore.

The main-board in the DOM contains two different digitizers to digitize the waveforms of the signal. They start acquiring data when a threshold on the voltage of approximately 0.25 times the typical voltage of a single photoelectron is reached. When the Analog Transient Waveform Digitizer (ATWD) is triggered by a voltage larger than the threshold, it will digitize the waveforms with a duration of 427 ns. The acquired data digitized by the ATWD within a specific

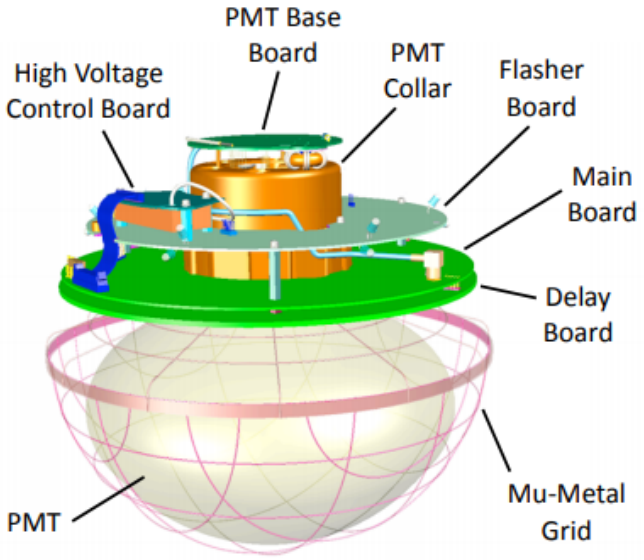

FIGURE 3.2: *Illustration of the digital optical module with the photomultiplier tubes pointing downward within the glass shell. From [11].*

DOM is discarded unless at least one neighbor or next-to-neighbor DOM on the same string is triggered as well within a 1000 ns window. The purpose of this is to reduce the noise, which will be discussed in Section 3.3. The fast Analog-to-Digital Converter (fADC) continuously digitizes and outputs waveforms within time windows of 6.4 ns.

The flasher board in the DOM contains 12 LEDs used for calibration. By emitting light, they are able to measure the positions of the DOMs and examine the properties of the ice. This is necessary when studying the absorption and scattering lengths of photons propagating through the detector. Information about the ice properties is crucial when processing the data acquired with IceCube [11].

3.2 Detection of neutrinos

It is not the neutrinos themselves that are detected by IceCube but rather the particles created when they interact in the ice at the South Pole. For this reason, neutrino interactions play an important role in the description of neutrino detection. This section will provide a description of neutrino interactions and what a neutrino looks like with the 'eyes' of IceCube.

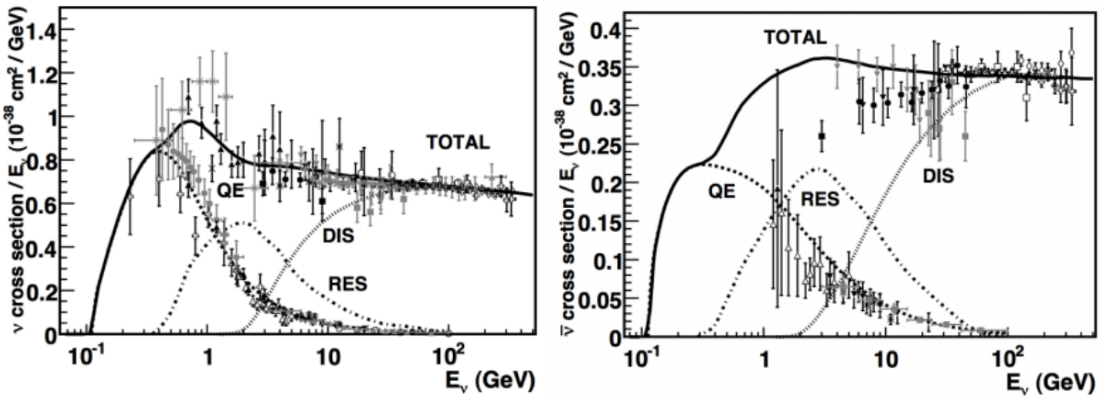

(A) (B)

FIGURE 3.3: *The plots show the neutrino (a) and antineutrino (b) cross section divided by the energy as a function of the energy for the CC interaction. Both the total and the individual contributions from the different processes, quasi-elastic (QE), resonant production (RES), and deep inelastic scattering (DIS), are shown. From [12].*

3.2.1 Neutrino interactions in matter

Neutrinos interact in the ice through the weak interaction by the exchange of a $W^{\pm}$ in a *charged current* (CC) interaction or of a Z^0 boson in a *neutral current* (NC) interaction. In the CC interaction there are three different interaction subtypes which dominate in different kinematical regimes, see Figure 3.3.

At low energies the CC interactions are dominated by quasi-elastic scattering (QE), where the incoming neutrino scatters off a whole nucleon that is left intact.

At intermediate energies of $\sim$1 GeV–10 GeV resonant production (RES) is dominating the CC interaction. In RES, the neutrino interacts with a nucleon forcing it into an excited baryonic state that subsequently decays to hadrons.

At higher energies — the energy regime relevant in this work — the neutrinos mostly participate in deep inelastic scattering (DIS) in CC as well as NC interactions [12]. Figure 3.4 shows these two types of DIS. In both cases, an incoming neutrino/antineutrino scatters off a nucleon present in the ice at the South Pole, with an energy high enough to hit one of the quarks inside. Subsequently, the nucleon shatters and emits a shower of hadrons — particles consisting of a quark and an antiquark pair (mesons) and/or particles consisting of three quarks (baryons). This is referred to as the *hadronic shower*.

In a NC interaction, the final state lepton remains a neutrino of the same flavor as the incoming neutrino. The final state neutrino propagates through the detector leaving no trace of the original neutrino flavor behind. In the CC

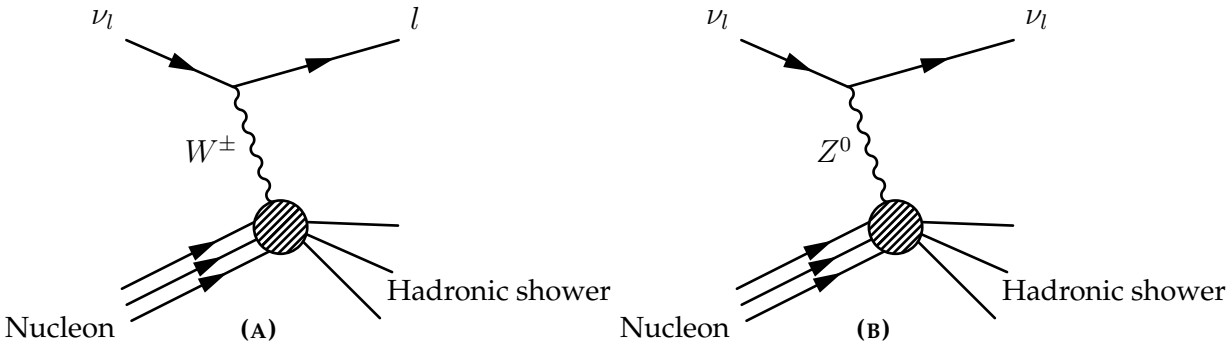

FIGURE 3.4: *(a) Feynman diagram of the CC interaction. A neutrino interacts with a nucleon through the exchange of a charged $W^{\pm}$ boson and is converted to a charged lepton in the process. (b) Feynman diagram illustrating the NC interaction, in which a neutral Z^0 particle is responsible for the incoming neutrino's interaction with the nucleon.*

interaction a charged lepton of the same flavor as the incoming neutrino is produced. The charged lepton can create a special signature revealing the flavor of the incoming neutrino. This will be discussed further in Section 3.2.3.

3.2.2 Cherenkov radiation

The IceCube neutrino telescope is a *Cherenkov detector* meaning that it detects the light emitted when charged particles propagate through the ice with a speed exceeding the speed of light in the ice. In general, the speed of light in a given medium, called the phase velocity v, is equal to the ratio between the speed of light in vacuum c and the refractive index n of the material,

$$v = \frac{c}{n}. \tag{3.1}$$

Typically, ice has $n \simeq 1.31$, which, using Equation 3.1, results in $v \simeq 0.76$c. This means that when a charged particle moves faster than $0.76c$ in ice Cherenkov radiation is emitted [13, 14]. The photons are emitted in a large range of wavelengths. The intensity increases with the wavelength and therefore the spectrum typically peaks at energies corresponding to the ultraviolet or blue part of the spectrum.

Cherenkov radiation occurs because a charged particle polarizes the ice but moves away before the medium has time to relax. This results in the production of wavefronts propagating in an angle θ relative to the particle's velocity, see Figure 3.5.

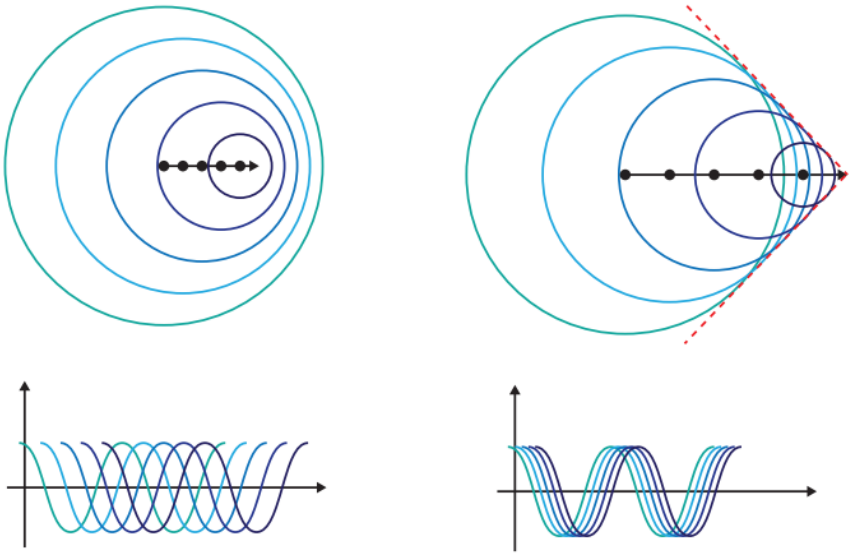

FIGURE 3.5: *Left panel: A charged particle polarizes the medium but moves slower than the polarization. Right panel: A charged particle polarizes the medium and moves faster than the speed of light in the given medium. In this case, a wavefront (red dashed line) is created and Cherenkov radiation will be emitted. From [15].*

The number of Cherenkov photons emitted increases with the travel distance of the charged particle. This means, that the longer the charged leptons produced via neutrino interactions travel through the ice, the more light will be created for the DOMs to detect, resulting in better angular reconstruction of the incoming neutrino.

3.2.3 Event topologies

An observed neutrino at IceCube is called an *event*. The topology of neutrino events can be very different depending on the neutrino flavor, its energy and the type of interaction. The topology is generally divided into two sub-groups: *tracks* and *cascades*. The names refer to the shape of the events, i.e., a track has a long track-like shape, while a cascade is shorter and has a more round shape.

NC interactions involving any neutrino flavor will produce cascades. In the NC interaction, the incoming neutrino is not converted into a charged lepton but rather stays a neutrino. Hence, there will be no particle to create a long track of Cherenkov radiation.

In the CC interaction of the electron neutrino an electron is produced in the final state. The electron will interact heavily with especially protons in the ice,

and consequently loses energy/slows down too rapidly to create a track-like topology.

Tracks are produced by incoming muon neutrinos interacting through the CC interaction. Muon neutrinos interacting through the exchange of $W^{\pm}$ bosons result in charged muons able to travel long distances in the ice before decaying or loosing too much energy to produce Cherenkov radiation. A long track of Cherenkov radiation in the detector will therefore generally be identified as a track originating from a muon neutrino CC interaction. However, if the muon energy is low and it's track is short, the neutrino might be misidentified as a different flavor, or the interaction is misidentified as a NC interaction.

In the CC interaction of an incoming tau neutrino, a charged tau lepton is created in the final state. The tau particle is very massive and therefore will decay too quickly to create a track. Instead, there will be one cascade from the production of the tau particle and another when the tau decays. In most cases the decay of the tau happens promptly after its production, leading to effectively a single cascade. However, in rare cases tau leptons with energies $\mathcal{O}$(PeV) may create the special "double bang" signature with two distinct cascades. Furthermore, in some cases, the taus created from the tau neutrino CC interaction will decay into a muon that subsequently creates a track-like signature in the detector, possibly leading to the neutrinos being misidentified as muon neutrinos.

3.3 Detector noise

In addition to the neutrino events described above, the detector also measures a signal originating from within the DOMs rather than Cherenkov photons. This is referred to as detector *noise*. The noise detected by the DOMs are divided into three subtypes: uncorrelated noise, correlated noise, and after-pulses, which have different origins and time profiles, see Figure 3.6 that is created using *HitSpool data*.

The HitSpool system is a buffer system used to store all hits in the DOMs for several hours. It was originally developed with the purpose of studying transient signals from supernovae, where the signal from each individual neutrino might be unable to trigger the data acquisition system (the digitizers). Consequently, the HitSpool data consist of untriggered raw data that have not been cleaned for noise. This property makes the HitSpool data excellent in the study of noise as well as supernovae.

The uncorrelated noise is created from thermal noise and radioactive decays in the PMTs. The time profile is Poisson distributed and depends on the temperature of the apparatus. Thus, the uncorrelated noise is different for DOMs

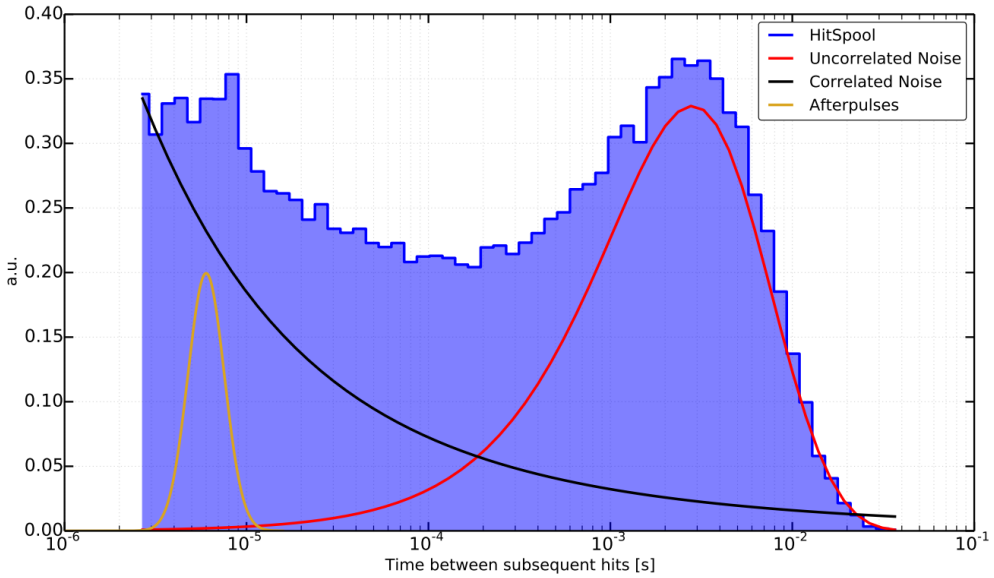

FIGURE 3.6: *Different components of the noise in the detector. Since only the relative shapes of the curves are important, the y-axis is in arbitrary units. From [16].*

deployed at different depths that operate at different temperatures.

The origin of correlated noise is still unknown. A possible explanation is luminescence within the glass of the pressure sphere, which may be triggered by radioactive decays. This component of the noise is measured as short bursts following a log-normal distribution.

The third subtype of the noise, the after-pulsing, is Gaussian of nature. It is created when electrons accelerated between dynodes within the PMTs ionize residual gases. Photocathodes attract the ions leading to free electrons that are subsequently measured in a process similar to the measurement of the original photoelectrons. Effectively, the after-pulsing is measured as a short Gaussian pulse arriving approximately 6 µs after the original signal.

If the signal of the noise exceeds the charge threshold of the DOMs, the detector noise will result in pure noise triggers, i.e., the ATWD will start acquiring data by digitizing the waveforms from the noise only. This makes noise cleaning necessary in order to obtain a clean signal from the neutrino events [11, 16].

Chapter 4

Astrophysical neutrinos and atmospheric background

Several types of astrophysical objects and phenomena are believed to emit neutrinos at both high and low energies. The *gamma-ray burst* is an example of such a source that is of particular interest for this analysis, and will be discussed more thoroughly in Section 4.1.1. Furthermore, the astrophysical neutrino production mechanism will be described in Section 4.2.

In addition to the astrophysical neutrinos of interest in the work, IceCube also detects an atmospheric background consisting of two components, atmospheric neutrinos and atmospheric muons. These two types of background will be discussed in Section 4.3.

4.1 Astrophysical neutrino sources

Our own Sun has already been mentioned as a neutrino source but other far more exotic and extragalactic sources are believed to exist as well. Most of these astrophysical objects are thought to emit neutrinos but are already known to emit electromagnetic radiation often in the form of gamma-rays. Some phenomena are even known to be powerful enough to bend space-time itself resulting in gravitational waves [17]. The possibility of observing neutrinos from those sources opens another dimension in *multimessenger astronomy*. By observing astrophysical objects through more than one type of messenger particle/wave, each one will provide its own unique information contributing to the total knowledge about the universe.

Neutrinos have the advantage of traveling in a straight line from their source to the Earth without being attenuated because they are electrically neutral and have an extremely small cross section. Effectively, this means that they will not

be deflected by electromagnetic fields or interact during their travels. These properties make the neutrino an almost perfect messenger particle, aside from the fact that the small cross section makes it very difficult to detect as well.

Gravitational waves are created in very energetic phenomena, e.g., in the collisions between neutron stars and/or black holes remaining after a core collapse supernova. Electromagnetic radiation have already been observed to coincide with gravitational waves from this type of phenomena. This was first observed in 2017 when two neutron stars collided approximately 40 Mpc from Earth [18]. However, neutrinos are still missing from the picture.

Neutrino sources with electromagnetic counterparts exist in different energy ranges and are of relevance for this work. This field of study remains relatively unexplored with only three objects observed through both messengers. These objects are our own Sun, the supernova 1987A, and the blazar TXS 0506+56. The supernova 1987A was the first extragalactic object to be observed through more than one messenger. It has been observed through photons as well as low-energy $\mathcal{O}$(MeV) neutrinos [19]. Most recently, high energy $\mathcal{O}$(100 TeV) neutrinos were associated with the blazar 0506+56, which was already observed across the entire electromagnetic spectrum [20].

Several analyses have been performed within IceCube with the purpose of searching for high-energy neutrinos in correlation with other messengers. However, analyses considering low-energy neutrinos are considerably less numerous. The most recent low-energy neutrino search for transient astrophysical point sources within IceCube was performed on a single year of data, consisting mainly of sub-TeV muon neutrinos originating from the Northern Sky [21]. No evidence of transient neutrino sources was found in the data, and an upper limit was placed on the neutrino emission from the targeted types of sources.

The gamma-ray burst is the astrophysical phenomenon of particular interest in the analysis performed in this work. Different theoretical models exist for gamma-ray bursts at different energy ranges, and in the low-energy case, there is a model both with and without the electromagnetic counterpart.

4.1.1 Gamma-ray bursts

Gamma-ray bursts are mostly of extragalactic origin. They are transient phenomena usually lasting between 0.1 and 1000 seconds. They are divided into two subgroups, namely the *short duration* and the *long duration* bursts. A gamma-ray burst is classified as a short burst if it last for up to 2 seconds, otherwise it belongs in the long duration subgroup. In this work, the focus will be on long gamma-ray bursts.

Gamma-ray bursts are not completely understood yet, however, several physical models do exist. One of the most commonly accepted models describing the

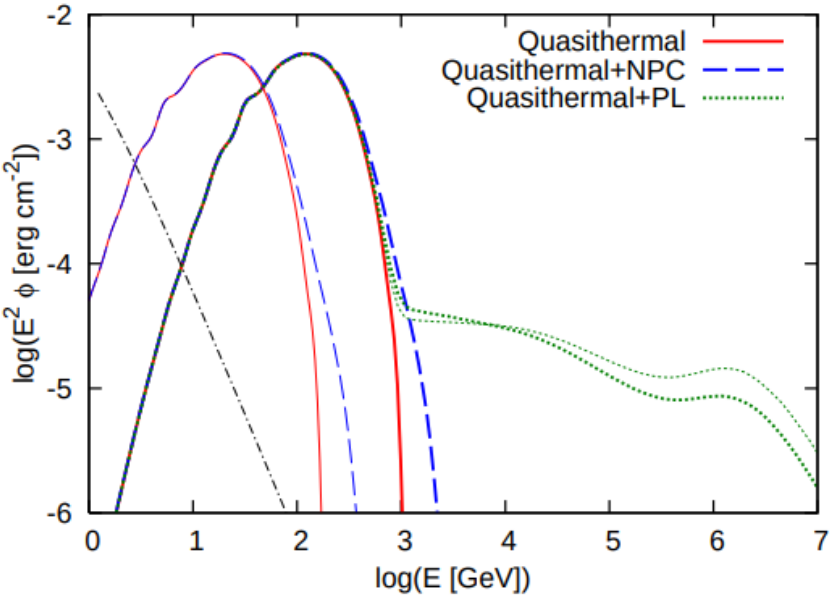

FIGURE 4.1: *Energy fluence of the high luminosity subphotospheric gamma-ray burst. From [23].*

long duration burst is called the *fireball model* [22]. According to this model, a compact rotating object is undergoing rapid accretion, which results in the production of relativistic jets along the object's axis of rotation. The compact object is either a black hole or a neutron star remaining after a core collapse supernovae. Material in the jets will be accelerated to relativistic velocities and the gamma-rays will break out of the stellar envelope surrounding the central object. The acceleration is caused by powerful magnetic fields that lead to Fermi acceleration. Sub-shells of material, e.g., protons, neutrons, and electrons, may be formed inside the fireball. These sub-shells will propagate with different velocities, which may create internal shocks. When one sub-shell overtakes another sub-shell, the particles going from upstream (faster sub-shell) to downstream (slower sub-shell) through the shock will gain energy. Thereafter, the charged particles may be reflected back through the shock into the upstream by magnetic fields, which will further increase its energy. This way, a charged particle can move back and forth between upstream and downstream repeatedly, while being significantly accelerated. The charged electrons will generate synchrotron emission observed as gamma-rays. The accelerated protons are responsible for the production of a neutrino flux (as will be described in Section 4.2), and thus the fireball model predicts neutrinos with energies $\mathcal{O}$(TeV).

Another model describing gamma-ray bursts and their neutrino emission

is the *subphotospheric model* [23]. The two models are similar in that they both contain a compact object in the center. However, in the subphotospheric model, the protons in the relativistic jets decouple from the neutrons, which causes the protons to reach higher velocities than the neutrons. Inelastic collisions between neutrons and protons in the early stages of the acceleration will lead to the production of e.g., pions. The neutrino emission is predicted to be at energies around $10\,\text{GeV}$–$100\,\text{GeV}$, i.e., much lower than in the fireball model. See Figure 4.1 for the energy fluence of the subphotospheric gamma-ray burst model.

A similarity between the two models, is that they both include the gamma-ray emission. This enables physicists to observe both gamma-rays and neutrinos from these astrophysical phenomena. Thus, detecting neutrinos originating from gamma-ray bursts is important for multimessenger astronomy.

Even though the gamma-ray emission from gamma-ray bursts have been observed multiple times related to the core collapse supernovae, most supernovae are observed without a subsequent gamma-ray burst. This has led to the idea of the *choked* gamma-ray burst where the jets fail to escape the stellar envelope. This may be a result of the jets not being energetic enough or the material surrounding the compact object being too dense. The small cross section of neutrinos will allow them to escape the envelope, resulting in an astrophysical object only observable through its neutrino emission [24].

4.2 Production of astrophysical neutrinos

The production of neutrinos in the gamma-ray burst models under consideration takes place after the material in the jets/photosphere are accelerated to high velocities. The protons may interact with the surrounding radiation in $p\gamma$*-interactions* (photo-meson production) or nucleons can interact in pp, np, nn*-interactions* (hadronuclear interactions). At the energies relevant for this work, pions are predominantly created from these interactions.

Hadronuclear interactions are of highest interest for the subphotospheric model [23]. In this scenario, protons and/or neutrons participate in internal inelastic collisions within the sub-shells producing both neutral and charged pions. Subsequently, the neutral pions decay in the following decay chain

$$\pi^0 \to \gamma\gamma, \tag{4.1}$$

resulting in a high energy gamma-ray flux but without contributing to the neutrino emission.

The charged pions decay in the following decay chains

$$\pi^+ \to \mu^+ + \nu_\mu, \tag{4.2}$$

followed by

$$\mu^+ \rightarrow e^+ + \nu_e + \bar{\nu}_\mu, \tag{4.3}$$

and

$$\pi^- \rightarrow \mu^- + \bar{\nu}_\mu, \tag{4.4}$$

followed by

$$\mu^- \rightarrow e^- + \bar{\nu}_e + \nu_\mu. \tag{4.5}$$

The resulting flavor ratio produced near the source is then $N_{\nu_e} : N_{\nu_\mu} : N_{\nu_\tau} = 1 : 2 : 0$, which can be counted directly from the reaction schemes. Thus, without oscillation we would expect to observe two muon neutrinos for every electron neutrino and no tau neutrinos. However, neutrinos do oscillate, cf. Section 2.2, and therefore the flavor ratio observed by IceCube will be different. Astrophysical neutrinos with the given flavor ratio of $N_{\nu_e} : N_{\nu_\mu} : N_{\nu_\tau} = 1 : 2 : 0$ will arrive at Earth with a ratio of $N_{\nu_e} : N_{\nu_\mu} : N_{\nu_\tau} = 1 : 1 : 1$ [25]. This result is illustrated in the flavor triangle in Figure 4.2.

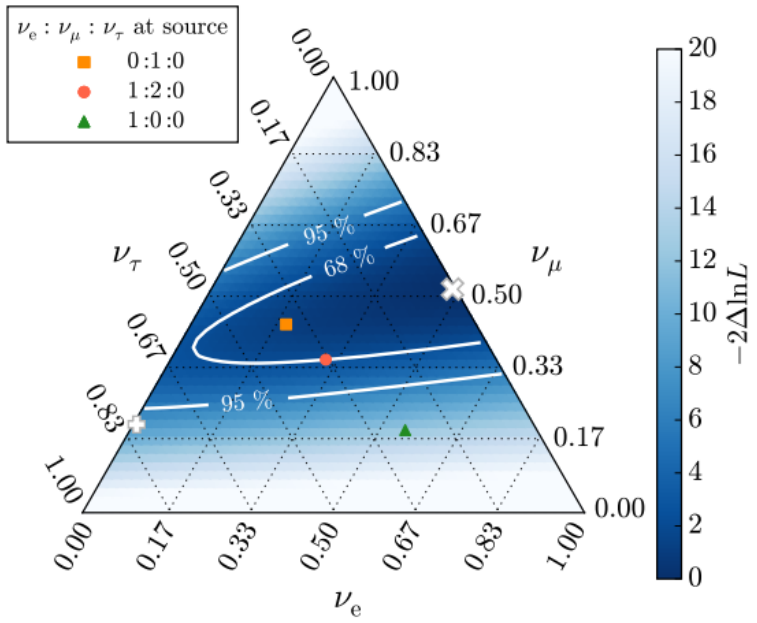

FIGURE 4.2: *Flavor triangle showing final neutrino flavor ratios for neutrinos produced with the initial flavor ratios (specified in legend) at an astrophysical source. The color scale is a profile likelihood scan made by Ref. [26] of the neutrino flavor composition at Earth. In this work, the red dot with an initial neutrino flavor ratio of 1:1:1 is relevant. Taken from [26].*

4.3 Atmospheric background

The atmospheric background is caused by cosmic rays interacting in the atmosphere. Cosmic rays consist mostly of high energy protons accelerated by astrophysical phenomena, e.g., by Fermi acceleration in gamma-ray bursts as described in Section 4.1.1. Although the discovery of cosmic rays is dating back more than a century [27], the specific origin and the acceleration mechanisms of the most energetic ones has not yet been fully established. Part of the lower energy cosmic ray flux can be accounted for by intergalactic supernovae and their remnants.

Cosmic rays are observed with energies across several orders of magnitude, as seen in Figure 4.3.

The primary cosmic ray particles collide and interact with nuclei in the upper atmosphere, a process where mainly charged pions and smaller amounts of kaons and heavier hadrons are created. Subsequently, the pions decay following decay chains similar to the ones described in Section 4.2, effectively resulting in a shower of secondary particles, as illustrated in Figure 4.4.

The atmospheric neutrino flavor ratio at low energies will be similar to the initial flavor ratio for the astrophysical neutrinos: $N_{\nu_e} : N_{\nu_\mu} : N_{\nu_\tau} = 1 : 2 : 0$, since the decay chains are the same. However, at neutrino energies of a few GeV,

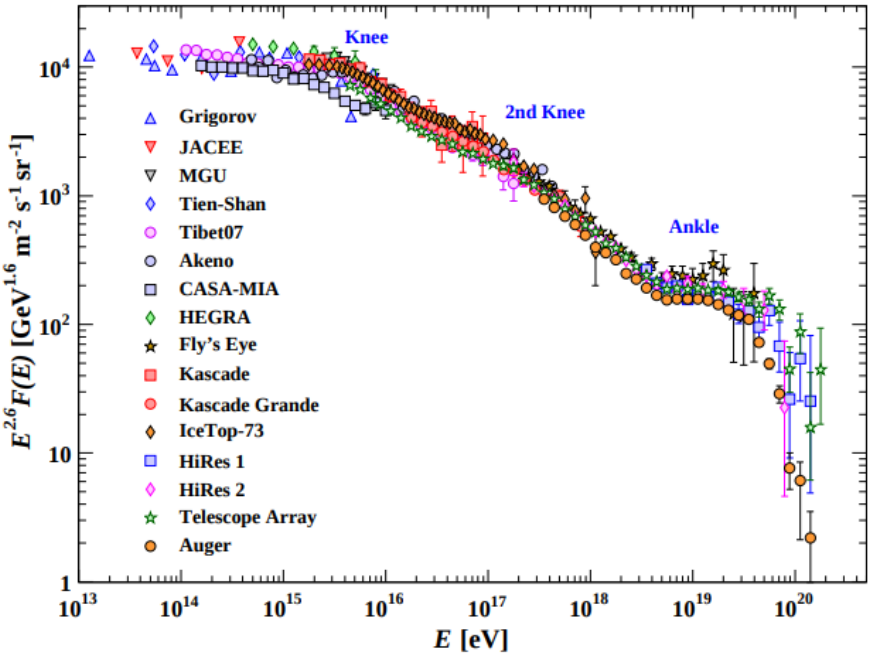

FIGURE 4.3: *Cosmic ray flux as a function of the energy per nucleon. From [28].*

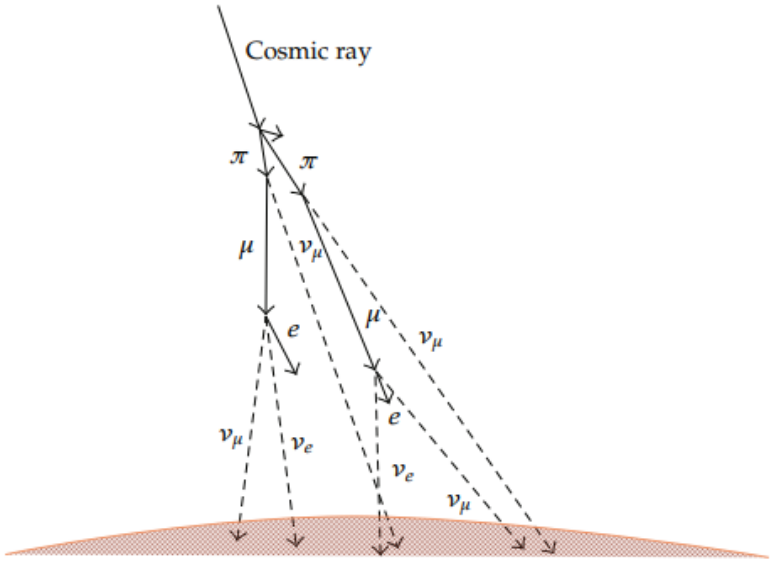

FIGURE 4.4: *Cosmic rays interact in the atmosphere resulting in a shower of secondary particles. From [29].*

the muons will start reaching Earth before having time to decay. Therefore, in this energy range, the contribution from electron neutrinos to the atmospheric neutrino flux will be suppressed and the atmospheric muon component will be detectable. Atmospheric neutrinos and muons will be described below.

Atmospheric muons created by cosmic rays have very large cross sections and short lifetimes compared to neutrinos. Therefore, muons with sufficiently high energies can reach the detector from the atmosphere but are unable to travel a long distance trough the Earth. Consequently, muons created in the atmosphere above the detector, on the southern hemisphere, are detectable, while muons created in the atmosphere on the Northern Hemisphere are incapable of reaching IceCube.

Seasonal fluctuations in the cosmic ray muon flux are the result of density changes of the atmosphere caused by temperature variations. For example, in warmer weather, the molecules in the air will rise up, leading to a more dense upper atmosphere and less dense lower atmosphere. Consequently, the pions are created at a larger altitude by the interactions of cosmic ray particles, and will have a decreased probability of interacting with air molecules before decaying into muons. This results in an increased cosmic ray muon flux reaching the Earth [30].

Low-energy atmospheric neutrinos are very abundant but the flux decreases

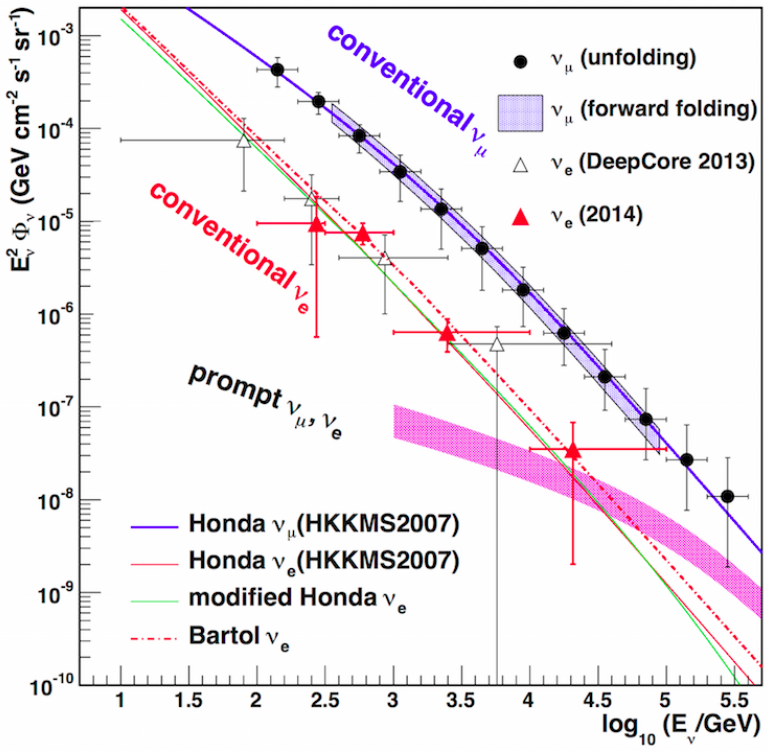

FIGURE 4.5: *Atmospheric neutrino flux as a function of the energy. From [32].*

rapidly with energy, as seen in Figure 4.5. The lines are theoretical predictions and the other markers are measurements performed by IceCube. The conventional neutrinos are those created in the air shower as described above. The purple band shows the prompt neutrino flux, which is predicted but not yet discovered. These neutrinos are emitted in the decays of the heavier mesons created in the interactions between cosmic rays and the nuclei in the atmosphere. The heavy mesons have a short lifetime and will decay promptly, hence the name *prompt neutrinos* [31].

Atmospheric muons traveling through the detector will leave a track-like signature just as a muon created via CC interaction of a muon neutrino. Atmospheric cosmic ray muons leave tracks immediately upon entering the detector, while muons created by neutrinos only leave tracks after the interaction of the neutrino. For this reason, cosmic ray muons are distinguishable from muons created by neutrinos within the detector. However, neutrinos traveling towards the detector but interacting in the ice outside of the detector will result in muons with signatures similar to those of cosmic ray muons.

Since it is impossible for muons to travel all the way through the Earth, a track-like signature originating from the Northern Hemisphere can always be

recognized as a muon emitted during neutrino interaction rather than a cosmic ray muon.

Chapter 5

Analysis

The objective in this work is to design and perform an analysis capable of discovering astrophysical transient point sources. A transient point source is characterized by only emitting neutrinos in a limited amount of time from a single point in the sky. Therefore, in order to observe this kind of source, the method/algorithm in the analysis should attempt to locate multiple neutrinos clustered in both time and space (multiplets). Since the focus in this analysis is on low-energy emission, the angular resolutions for the events are lower than for high energy neutrinos in IceCube. Thus, events emitted from a low-energy point source will be distributed over a relatively large area on the sky. This results in the need of observing multiple neutrino events in order to make a qualified guess on the true position of the source.

This analysis will contain two parts: A kernel density estimate (KDE) in time with the purpose of locating the times with the largest densities of events, followed by an unbinned maximum likelihood method that tests for spatial clustering.

The event selection used in this search is described in Section 5.1.1. Section 5.1.2 offers a description of how the background and signal data is modeled. In Section 5.2 the KDE is explained in detail, while Section 5.3 is dedicated to a description of the maximum likelihood method. The performance of the analysis is presented in Section 5.4. Finally, Section 5.5 provides a discussion on some of the choices made while designing the analysis and setting the parameters, including how some values can be optimized differently in the framework of the future real-time search.

5.1 Data sample for background and signal

This section is dedicated to a description of the properties and utilization of the dataset used in this analysis.

5.1.1 The GRECO event selection

In this analysis, the GeV Reconstructed Events with Containment for Oscillations (GRECO) event selection is used. This is a low-energy data sample that was originally developed for, and used in, the recent IceCube tau appearance oscillation analysis [33]. GRECO contains events in the energy range ∼10 GeV–1000 GeV that are therefore detected mainly by the low-energy extension IceCube-DeepCore.

GRECO is the event selection resulting from applying cuts in seven different levels. The purpose of the cuts is to remove accidental triggers originating from detector noise as explained in Section 3.3 and atmospheric muons created by cosmic rays described in Section 4.3. Figure 5.1 shows how the event rate decreases as a function of the cuts within the different levels. Before applying any cuts, the total rate is approximately 1 kHz and is by far dominated by atmospheric muons. After Level 1, the rate of atmospheric muons is comparable to that of accidental noise triggers. At Level 6 the muon neutrino flux exceeds both the atmospheric muon flux and the rate of noise triggers. At the final level, Level 7, which is used in this work, the total rate decreased to approximately

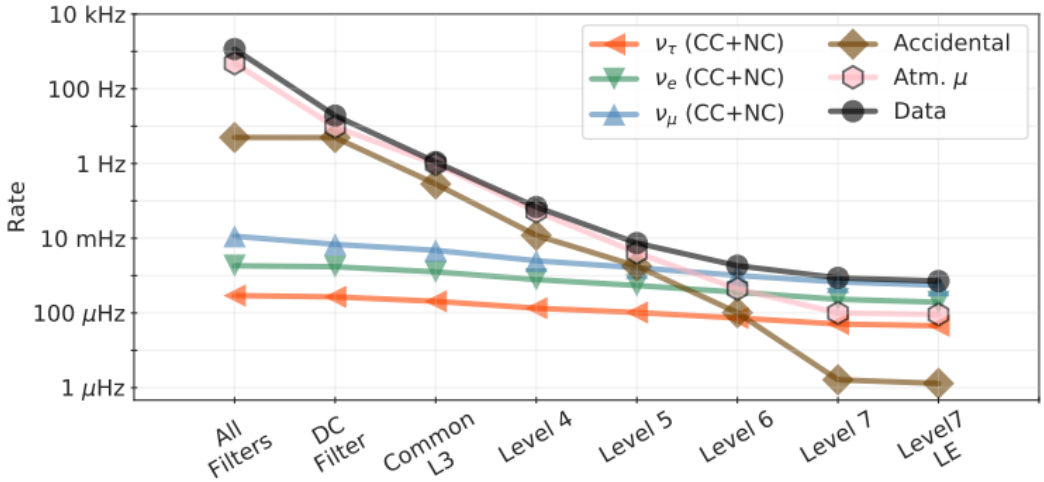

FIGURE 5.1: *Components contributing to the rate of GRECO events at different levels, with the black curve indicating the sum of individual contributions. Taken from [33].*

1 mHz and is dominated by muon and electron neutrinos. The rate of tau neutrinos is slightly lower than that of atmospheric muons. The accidental triggers from noise are negligible with a rate two orders of magnitude smaller than the rates of the other components.

The effective area of the GRECO dataset surpasses that of all other available datasets at energies up to ∼150 GeV, which makes it the best possible choice for a low-energy astrophysical search, although it was originally developed for an oscillation analysis. The total full sky effective area for the GRECO event selection used in this analysis is shown in Figure 5.2a (black, dashed line) together with the individual contributions from the three neutrino flavors (solid lines). This is compared to the effective area of the previous low-energy analysis [21] performed within IceCube, cf. Section 4.1. The effective area in this work is larger at low energies, because this is a full sky search including all neutrino flavors and both event topologies, tracks and cascades, as opposed to the previous search that considered tracks created by muon neutrinos from the Northern Sky only.

Figure 5.2b shows the effective area for the GRECO sample for three wide declination bands. The effective area for GRECO increases with declination because more events originating from the Northern Hemisphere (with positive declinations) remain in the final dataset after performing the event selection as compared to events originating from the Southern Hemisphere. This is a result of cosmic-ray muon events being indistinguishable from some neutrino events from the Southern Sky, which causes these neutrino events to be classified as atmospheric muons leading them to be removed during the event selection, as discussed in Section 4.3.

5.1.2 Modeling background and signal

Time scrambled experimental GRECO data is used as background, because it consists manly of atmospheric neutrinos, which provides the most realistic background possible. When scrambling the times, the events are uniformly distributed within the livetime of the dataset. Distributing the events only within the livetime assures that the correct rate is achieved. Anisotropies in time and azimuth/right ascension are averaged out when scrambling the data uniformly in time. This is a simplification but is reasonable since the background rate only varies up to ∼15% around the mean in both time and azimuth as seen in Figure 5.3. How these fluctuations in the background rate affects the performance of the analysis will be discussed later and it will be accounted for in the final results as systematic uncertainties.

A signal neutrino fluence corresponding to a source is modeled using simulated GRECO data. The chosen signal events are injected in the background

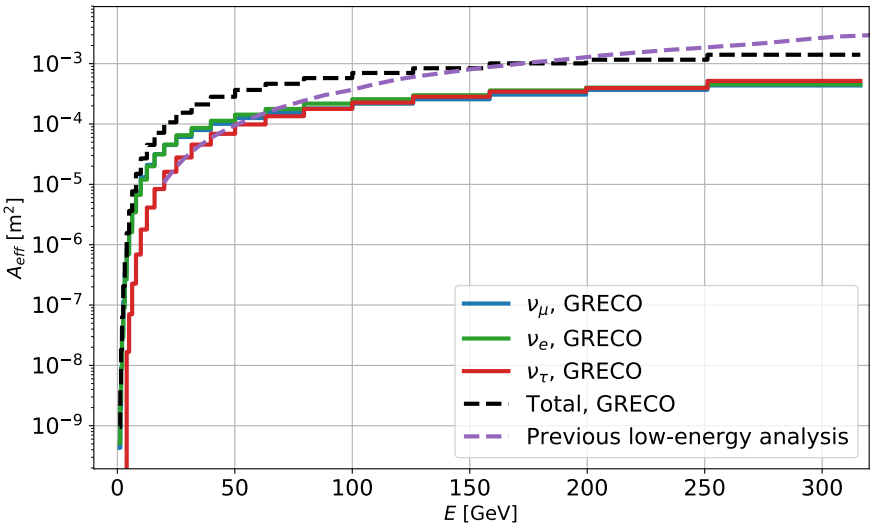

(A)

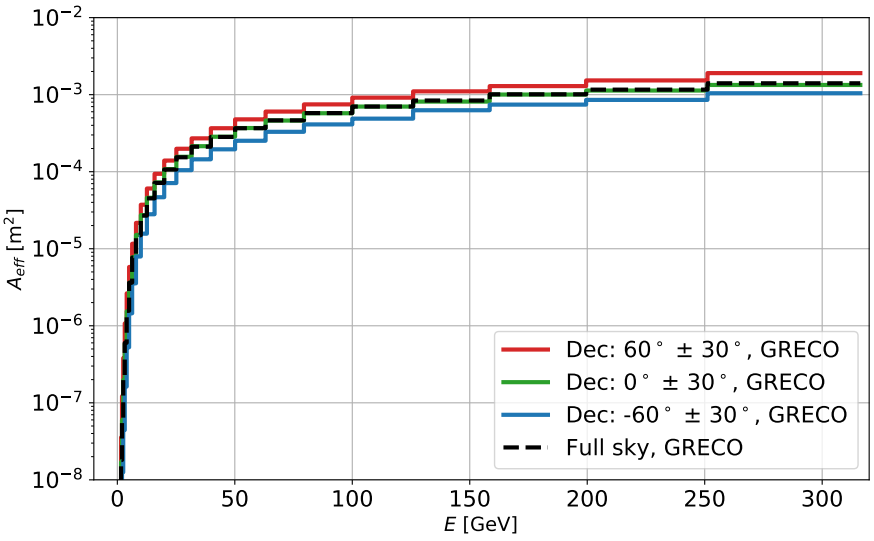

(B)

FIGURE 5.2: *(a) The full sky all flavor effective area (black dahed line) and the contributions from individual neutrino flavors (solid lines). This is compared to the effective area of the of previous low-energy analysis (purple dashed line) [21]. (b) The all flavor effective area for different declination bands for the GRECO event selection (solid lines) and the average over the whole sky (black dashed line).*

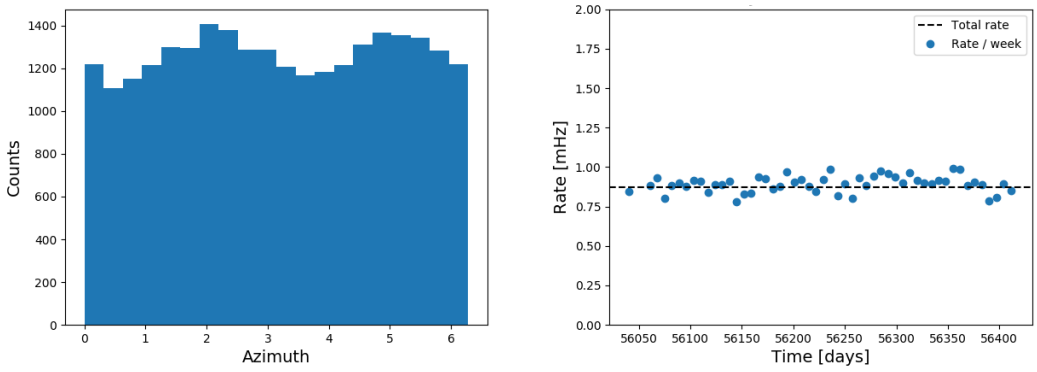

(A) (B)

FIGURE 5.3: *(a) Azimuth distribution and (b) rate as a function of time for one year of unscrambled GRECO data from 2012.*

data following a specific energy spectrum corresponding to the subphotospheric model for gamma-ray bursts, cf. Section 4.1.1. The fluence approximated by the Fermi-Dirac distribution is parameterized by

$$\Phi(E) = \mathcal{N} \cdot \frac{\left(\frac{E}{kT}\right)^2}{e^{\frac{E}{kT}} + 1}, \tag{5.1}$$

where E is the energy, $\mathcal{N}$ is the normalization that depends on the strength of the source, and kT is Boltzmann's constant multiplied by the temperature. The mean energy of the source is given by

$$\langle E \rangle = 3.15kT. \tag{5.2}$$

In this work, mean energies of 20 GeV (SPS20) and 100 GeV (SPS100) are used as benchmarks, see Figure 5.4.

The number of injected signal events is correlated with the source fluence and determines the strength of the source. The injection follows a Poisson distribution. This means that all indicated numbers of signal events throughout this work, refer to the mean of a Poisson distribution where the actual numbers of signal events are drawn from, unless otherwise specified. This ensures that a fractional number can be chosen as the Poisson mean, while the actual number of injected events always is an integer.

The neutrino emission time for the astrophysical sources under consideration in this work (gamma-ray bursts) is unknown. No models describe the neutrino emission time theoretically and no observations have been able to shed light on this property of the sources either. Hence, in this work, the neutrino

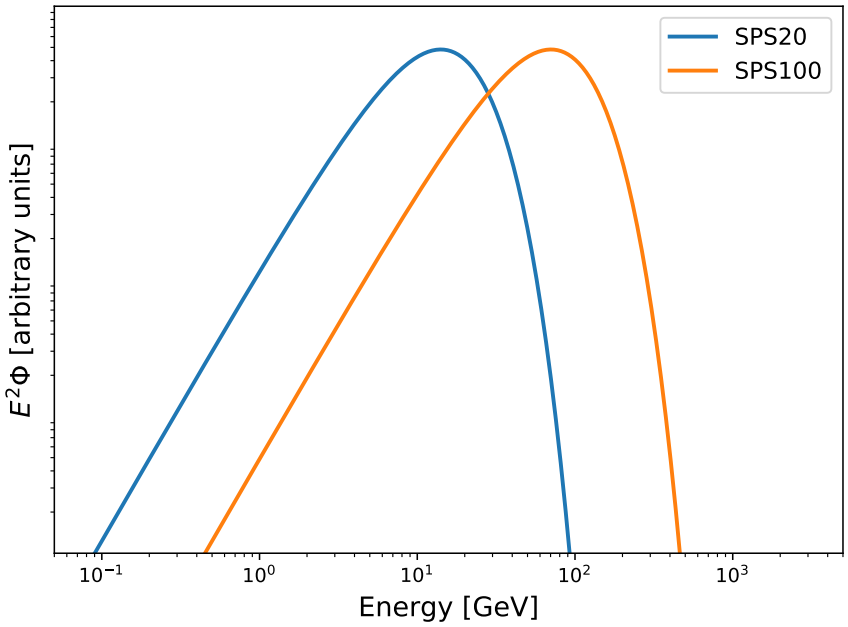

FIGURE 5.4: *Shape of subphotospheric energy spectra modeled according to a Fermi-Dirac spectrum with mean energies of 20 GeV and 100 GeV. The y-axis is arbitrary since the normalization is unknown.*

emission is assumed to be correlated with the well-known gamma-ray emission. Therefore, as an approximation, the signal events are normal distributed with a standard deviation of 100 s around a randomly chosen time.

The true spatial position of the injected source is chosen and signal events are chosen by random from a narrow declination band of $\pm 3^\circ$ around the true source declination. The true simulated position of each chosen event is shifted to the true source position and the events are injected at their corresponding reconstructed coordinates after undergoing the shift, see Figure 5.5 for an illustration.

By taking the angle between the true and reconstructed positions of the events into account a realistic injection is ensured, because the events will be injected at a realistic angular distance to the source.

The events are injected with a final flavor ratio of $N_{\nu_e} : N_{\nu_\mu} : N_{\nu_\tau} = 1 : 1 : 1$ after oscillation, cf. Section 4.2. Choosing the correct flavor ratio for the source type under consideration is crucial, because the relative number of tracks and cascades depends on the flavor ratio, which influences both the injection of signal events and the angular resolutions assigned to the events. If the flavor ratio is wrong and the signal for example contains an excessive number of muon

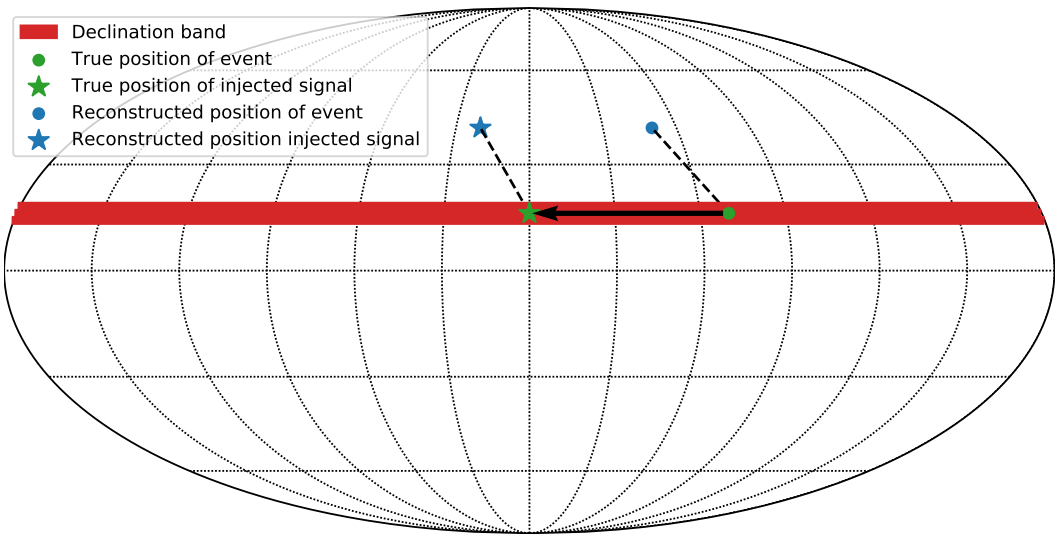

FIGURE 5.5: *Sky map to illustrate the injection method of signal events. The true position of the source (green star) is chosen and the desired number of events with their true positions within the band are selected (green dot). True and reconstructed positions of events (green and blue dots) are shifted together in order to make the true event positions overlap with the true source position. Finally, the event is injected at its reconstructed position (blue star).*

neutrinos, the signal will contain too many tracks. This will result in better angular resolutions, effectively causing the events to be injected too close to the true source position on average, which will lead to more prominent spatial clustering.

5.2 Kernel density estimation

The first part of the analysis is the kernel density estimation with the purpose of locating times with large densities of events. Only the most promising times with event densities above a given threshold are selected and time windows are created around these times. The spatial maximum likelihood analysis is only performed on the events within the time windows, meaning that the KDE works as a preselection of events before the maximum likelihood is used. Since the dataset consists mainly of atmospheric neutrino background, it is pointless to use an excessive amount of computing power to perform a spatial analysis on all events.

The essential principle of the time KDE is to create a Gaussian *kernel* in time for each event and add the contributions together for all events. The kernel

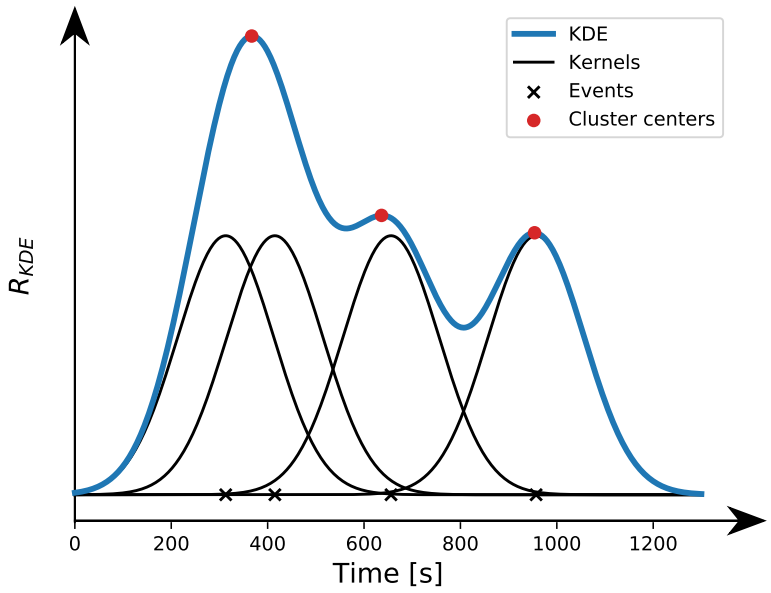

FIGURE 5.6: *Illustration to show the principle of the time KDE with a bandwidth of 100 s for each kernel, with the maxima of the KDE indicated by red dots (cluster centers).*

is basically a Gaussian PDF (it integrates to 1) centered around the observation time for events. The sum of all kernels is then a measure of the density of events. Figure 5.6 shows an illustrative, constructed example of four "events" together with the sum of the individual contributions from the kernels. The times of interest are the maxima of the KDE, which is referred to as *cluster centers*.

The kernel can in principle take different shapes and the bandwidth can be optimized in different ways depending on the analysis. In this analysis, the choice of bandwidth is based on the physics of the astrophysical sources and should correspond to the neutrino emission time. Consequently, the bandwidth is 100 s seconds wide.

In general, a KDE is a data driven probability density, however in this work, the objective is to estimate the unnormalized density, because the analysis should work independently of the number of events. Hence, the sum of kernels is used without further normalization, and its value is referred to as R_{KDE}.

After performing the time KDE (summing the kernels), all cluster centers are found. The cluster centers with a value of R_{KDE} above a given threshold are then chosen as the most likely times for the transient neutrino emission from possible sources. A time window of ± 3 bandwidths (600 s in total) is created

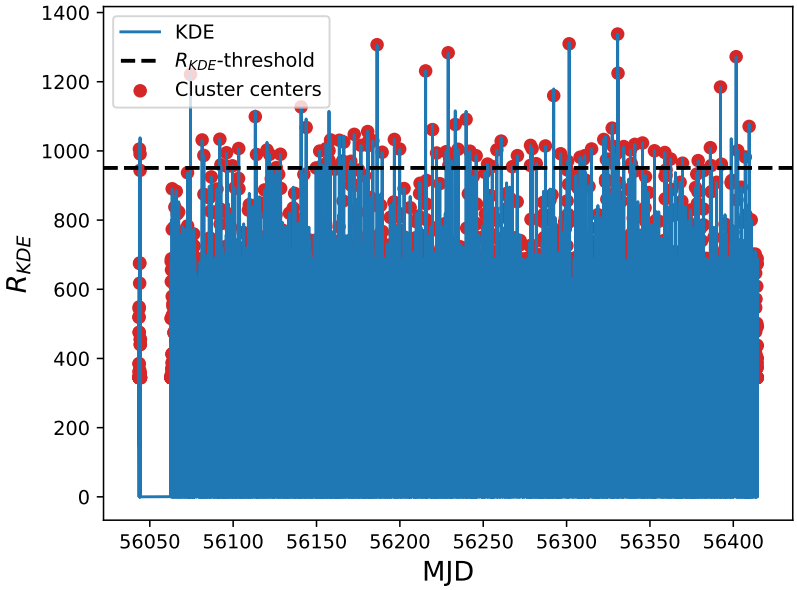

FIGURE 5.7: *Time KDE for one year of scrambled data (2012). The x-axis is in days (Modified Julian Date counting the number of days since November 17, 1858). The dashed line corresponds to the R_{KDE}-threshold above which there will be an average of 100 cluster centers per year, i.e., this threshold will result in N_{TWPT} =100.*

around each chosen cluster center above the $R_{KDE}-$threshold. The average expected number of time windows will be referred to as N_{TWPT} (TWPT=Time Window with Potential Transients). The $R_{KDE}-$threshold is independent of the number of events, since the unnormalized density is used. Furthermore, it is correlated with the value of N_{TWPT}. Therefore, the value of the R_{KDE}-threshold can be chosen to result in a specific average N_{TWPT} for a given year of data. In this work, R_{KDE}-threshold=950.80 is chosen corresponding to N_{TWPT}=100, i.e., the threshold will allow 100 cluster centers to pass per year on average. Figure 5.7 Shows an example for one year of scrambled GRECO data.

For each time window, the spatial maximum likelihood analysis is performed on the selected events within.

5.3 Maximum likelihood

An unbinned maximum likelihood analysis is performed using the events within each time window, i.e., the events within ± 3 bandwidths around each time KDE

cluster center passing the R_{KDE}-threshold. The likelihood contains spatial information about the events, and can therefore be used to estimate their spatial clustering. The amount of spatial clustering between the events is either indicative of neutrinos from a point source or of atmospheric neutrino background.

In this section, the likelihood function used in the analysis is defined, then a relatively simple expression for the natural logarithm to the likelihood ratio is derived. Subsequently, the signal and background probability distributions are described followed by a discussion of the maximization.

5.3.1 Likelihood function

In order to create an expression for the likelihood function, consider an astrophysical source featuring neutrino emission. The total number N of neutrinos from the source observed by IceCube follows a Poisson distributed probability [34]

$$P(n_s) = \frac{(n_s + n_b)^N}{N!} e^{-(n_s+n_b)}, \tag{5.3}$$

where n_s and n_b are the number of signal and background neutrinos within a given time window, respectively. The likelihood for each event i is given by

$$\mathcal{L}_i(n_s) = \frac{n_s \mathcal{S}_i}{n_s + n_b} + \frac{n_b \mathcal{B}_i}{n_s + n_b}, \tag{5.4}$$

with $\mathcal{S}_i$ and $\mathcal{B}_i$ being the probability distribution functions (PDF's) for signal and background for the event i. Meaning that for a given neutrino event, $\mathcal{S}_i$ describes the probability of that event originating from a transient point source and thereby being a signal neutrino, and $\mathcal{B}_i$ is the probability of the event being a background event that does not originate from the source. The expressions will be discussed in detail in the following sections.

The total likelihood is obtained by multiplying together the different contributions,

$$\mathcal{L}(n_s) = P(n_s) \prod_{i=1}^{N} \mathcal{L}_i(n_s) = \frac{(n_s + n_b)^N}{N!} e^{-(n_s+n_b)} \prod_{i=1}^{N} \left(\frac{n_s \mathcal{S}_i}{n_s + n_b} + \frac{n_b \mathcal{B}_i}{n_s + n_b} \right). \tag{5.5}$$

In order to test whether or not a given time window contains signal events from an astrophysical source, a null-hypothesis H_0 and an alternative hypothesis H_1 are formulated.

> **H_0:** No signal events are present in the given time window. The time window contains background only.

$\mathbf{H_1}$: The events within the given time window are a combination of signal and background neutrinos.

The likelihood for the alternative hypothesis being true is given by $\mathcal{L}(n_s)$ defined by Equation 5.5, while the likelihood for the null hypothesis is denoted $\mathcal{L}(0)$. The objective of the maximum likelihood analysis is to estimate how much more likely it is for a time window to contain signal events (follow the alternative hypothesis), rather than containing background only (follow the null hypothesis). This can be estimated using the natural logarithm of the likelihood ratio, which is written as

$$\begin{aligned}
\ln\left(\frac{\mathcal{L}(n_s)}{\mathcal{L}(0)}\right) &= \ln\left(\frac{\frac{(n_s+n_b)^N}{N!}e^{-(n_s+n_b)}\prod_{i=1}^{N}\left(\frac{n_s\mathcal{S}_i}{n_s+n_b}+\frac{n_b\mathcal{B}_i}{n_s+n_b}\right)}{\frac{n_b^N}{N!}e^{-n_b}\prod_{i=1}^{N}\mathcal{B}_i}\right) \\
&= \ln\left(\frac{\frac{(n_s+n_b)^N}{n_b^N}e^{-n_s}\prod_{i=1}^{N}\left(\frac{n_s\mathcal{S}_i}{n_s+n_b}+\frac{n_b\mathcal{B}_i}{n_s+n_b}\right)}{\prod_{i=1}^{N}\mathcal{B}_i}\right) \\
&= \ln\left(\left(\frac{n_s+n_b}{n_b}\right)^N e^{-n_s}\prod_{i=1}^{N}\left(\frac{n_s\mathcal{S}_i}{(n_s+n_b)\mathcal{B}_i}+\frac{n_b}{n_s+n_b}\right)\right).
\end{aligned} \tag{5.6}$$

The logarithm of products can be rewritten in terms of sums. This yields

$$\ln\left(\frac{\mathcal{L}(n_s)}{\mathcal{L}(0)}\right) = \ln\left(e^{-n_s}\right) + \ln\left(\left(\frac{n_s+n_b}{n_b}\right)^N\right) + \sum_{i=1}^{N}\ln\left(\frac{n_s\mathcal{S}_i}{(n_s+n_b)\mathcal{B}_i}+\frac{n_b}{n_s+n_b}\right). \tag{5.7}$$

The logarithm and the exponential function cancel out in the first term, and the logarithmic rule

$$\ln(x)^y = y\ln(x),$$

is used to simplify the second term. Further, the summation rule

$$\ln(x+y) = \ln(y) + \ln\left(1+\frac{x}{y}\right),$$

is used to rewrite the last term. Equation 5.7 can then be written as

$$\ln\left(\frac{\mathcal{L}(n_s)}{\mathcal{L}(0)}\right) = -n_s + N\ln\left(\frac{n_s+n_b}{n_b}\right) + \sum_{i=1}^{N}\left(\ln\left(\frac{n_b}{n_s+n_b}\right) + \ln\left(1+\frac{n_s\mathcal{S}_i}{n_b\mathcal{B}_i}\right)\right). \tag{5.8}$$

The first term in the summation is independent of i and can therefore be placed outside by multiplying with N. This gives

$$\ln\left(\frac{\mathcal{L}(n_s)}{\mathcal{L}(0)}\right) = -n_s + N\ln\left(\frac{n_s+n_b}{n_b}\right) + N\ln\left(\frac{n_b}{n_s+n_b}\right) + \sum_{i=1}^{N}\ln\left(1+\frac{n_s\mathcal{S}_i}{n_b\mathcal{B}_i}\right). \quad (5.9)$$

The second and third term can again be rewritten to the logarithm of the product of the parentheses, which causes them to cancel. The value of n_b is estimated from the data as the expected number of background events in a time window, calculated as the background rate times the length of the time window. This will be denoted $\langle n_b \rangle$. The final expression for the log-likelihood ratio is then obtained

$$\ln\left(\frac{\mathcal{L}(n_s)}{\mathcal{L}(0)}\right) = -n_s + \sum_{i=1}^{N}\ln\left(1+\frac{n_s\mathcal{S}_i}{\langle n_b\rangle\,\mathcal{B}_i}\right). \quad (5.10)$$

Equation 5.10 is the expression used in the likelihood analysis. The spatial background and signal PDF's will be described in the following sections.

5.3.2 Background PDF

The background PDF $\mathcal{B}_i$ for a given event in a time window describes the probability of that event originating from the background. It is given by the probability of observing a background event in the specific position of the given event. Hence, it depends on the position of the event, i.e., declination and right ascension. However in this work, a uniform distribution of events in right ascension is assumed, since the anisotropies in time and azimuth shown in Figure 5.3 are averaged out, cf. Section 5.1. Therefore $\mathcal{B}_i$ is a function of the declination only.

The value of $\mathcal{B}_i$ is calculated as a product of the probability $\mathcal{P}_{i,dec}$ of observing the event at a given declination and the probability $\mathcal{P}_{i,right\ ascension}$ of observing the event at a given right ascension, where the latter is a constant.

$$\mathcal{B}_i = \mathcal{P}_{i,dec}\cdot\mathcal{P}_{i,right\ ascension} = \mathcal{P}_{i,dec}\cdot\frac{1}{2\pi}. \quad (5.11)$$

Since there are 2π radians in right ascension the probability of observing an event at a specific point is $\frac{1}{2\pi}$. The probability of an observation at a given point in declination is estimated from data. The background distribution of events in cos(zenith) is shown in Figure 5.8. Based on the distribution a spline is created and used to find $\mathcal{P}_{i,dec}$ for each event.

As seen in Figure 5.8, the variations in cos(zenith) are very large compared to the fluctuations in azimuth as seen in Figure 5.3. Hence, although the small

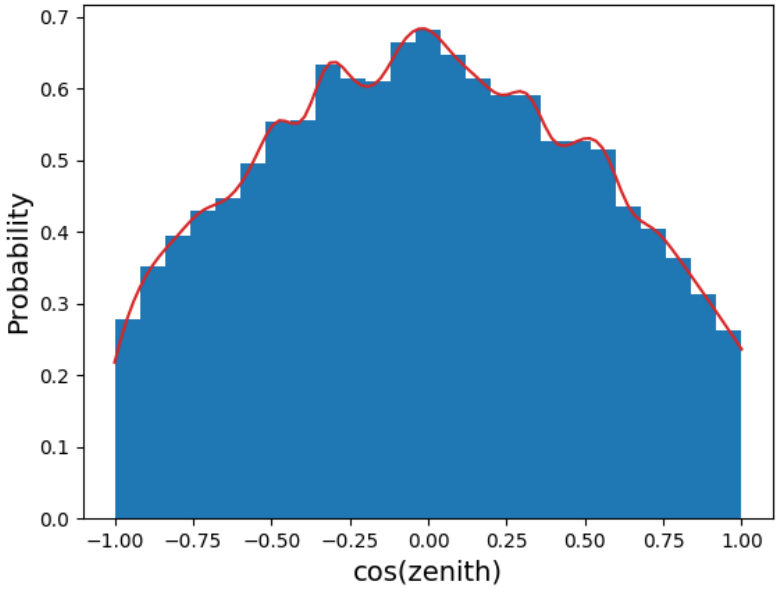

FIGURE 5.8: *Background event distribution as a function of cos(zenith). The spline used in the expression for the background PDF is drawn in red.*

fluctuations in azimuth/right ascension is averaged out and just included as systematic uncertainties in the final results, the larger variations in declination will be accounted for in the background PDF $\mathcal{B}_i$.

When using the experimental data to estimate the background PDF, it is assumed that no or very little signal neutrino emission originating from point sources is present in the data. If the data contained a significant amount of signal neutrinos form point sources, it would be unable to accurately describe the probability distribution of background events.

5.3.3 Signal PDF

The signal PDF $\mathcal{S}_i$ describes the probability of a given event originating from an astrophysical source. It should therefore be a function of the angular distance between a possible source location and the event i as well as the angular resolution of the event. In principle, the angular extent of the source could be taken into account, but since the analysis designed and performed in this work is a point source search the angular extent is assumed to be zero.

In this work a Kent distribution [35] is used to model the signal PDF. This is essentially the spherical counterpart of a two-dimensional Gaussian, i.e., a two

dimensional Gaussian normalized to the surface of a sphere. Assuming circular event angular uncertainties, meaning that the uncertainty in declination is equal to the uncertainty in right ascension, the Kent distribution takes the form

$$\mathcal{S}_i = \frac{\kappa_i}{4\pi \sinh(\kappa_i)} e^{\kappa_i \cos(|x_{source} - x_i|)}, \tag{5.12}$$

where $|x_{source} - x_i|$ is the angular separation between a possible source location and a given event. The parameter κ denotes the concentration parameter of the Kent distribution, which is related to the angular uncertainty σ_i for the event through

$$\kappa_i = \frac{1}{\sigma_i^2}. \tag{5.13}$$

The true coordinates for the experimental data are unknown, as opposed to the simulated data where both the true and reconstructed coordinates are known. Therefore the angular resolutions can be calculated as the angular distance between the true and reconstructed positions for the simulated data. The angular resolutions for experimental data are therefore parameterized using the simulated data, by creating two splines of the median angular spread between the true and reconstructed positions as a function of the energy and declination. There are two separate splines created relating to the two different event topologies in the GRECO sample, tracks and cascades. Tracks are generally reconstructed better, which is reflected in the splines, and consequently, more accurate estimates of the angular uncertainties are achieved by taking the event topology into account. This separation between tracks and cascades is done with a particle identification (PID).

The PID in the GRECO event selection classifies events as tracks when their a reconstructed track-length is more than 50 m, while events are classified as cascades if their track-length is smaller than 50 m. This means that some tracks with short track-lengths ($<$50 m) are misidentified as cascades and some cascades with longer track-lengths ($>$50 m) are misidentified as tracks. However, tracks with small track-lengths have a worse angular reconstruction than tracks with longer track-lengths, and similarly, cascades with long track-lengths have a better angular reconstruction compared to cascades with smaller track-lengths. This is reflected in the splines when using this PID, and therefore not a lot of information is lost this way.

When creating the splines using the simulated data, the events are weighed according to the expected energy spectrum for atmospheric neutrinos as described in Ref. [36]. This ensures that the splines are weighed correctly for the majority of the events, since the background consists mainly of atmospheric neutrinos.

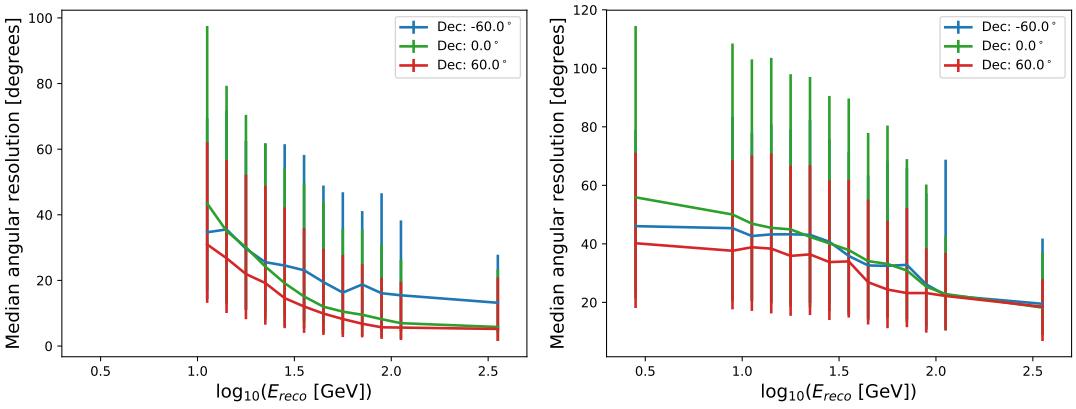

FIGURE 5.9: *The median angular resolution for (a) tracks and (b) cascades defined as the angular spread between the true and reconstructed positions of simulated data events. Error bars indicate the 68% central intervals. Declinations specified in the legend refer to the bin centers.*

Figure 5.9 shows the median angular resolution as a function of the energy for a few example declination bins. From the figure, it is seen that the angular resolution, in general, is better for tracks than cascades as expected, since tracks leave a longer trail of Cherenkov photons through the detector. Furthermore, the angular resolution is improving with neutrino energy since the higher energy neutrinos create more photons when interacting in the ice and therefore the DOMs will measure a stronger signal. This leads to better reconstruction of the event positions. Likewise, the angular resolution is in general better for events with positive declinations, as a result of the DOMs pointing downward, which enables them to measure more photons from neutrinos originating from the Northern Hemisphere.

Bins are distributed linearly in declination between -85 and 85 degrees with a bin-width of five degrees (only a few are shown on the plots). A few degrees are left out around the poles because these bins otherwise would contain very few or no events, potentially resulting in outliers. By leaving out the few degrees closest to the poles, too much weight on single/few simulated events is avoided, ensuring that the splines are based on the majority of the data.

Energy bins are slightly different for cascades and tracks. For cascades, 12 bin centers are distributed logarithmically in the range $\sim$8.9–112.2 GeV, with two additional bin centers at $\sim$2.8 GeV and $\sim$354.8 GeV in order to include the lowest and highest energy neutrinos. These two additional bins are wider than the other bins on the log-scale. The energy bins for tracks are similar, except that

the first two bins are removed because no tracks have a reconstructed energy below ∼10 GeV, due to the requirement that tracks are at least 50 m long.

5.3.4 Maximization

The signal and background PDFs have been described, meaning that all components of the log-likelihood ratio in Equation 5.10 are well-defined. The log-likelihood ratio is then maximized with respect to the parameter n_s and the source coordinates included in the signal PDF. In this way, a likely source position is found along with the number of events in the time window likely to originate from that particular source. The parameter n_s is constrained to be a fraction of the total number of events within the time window.

In addition to the R_{KDE}-threshold, another threshold is applied on the fitted value of n_s. This threshold is set to 2 in order to require a minimal amount of spatial clustering. This is necessary because a single event with very good

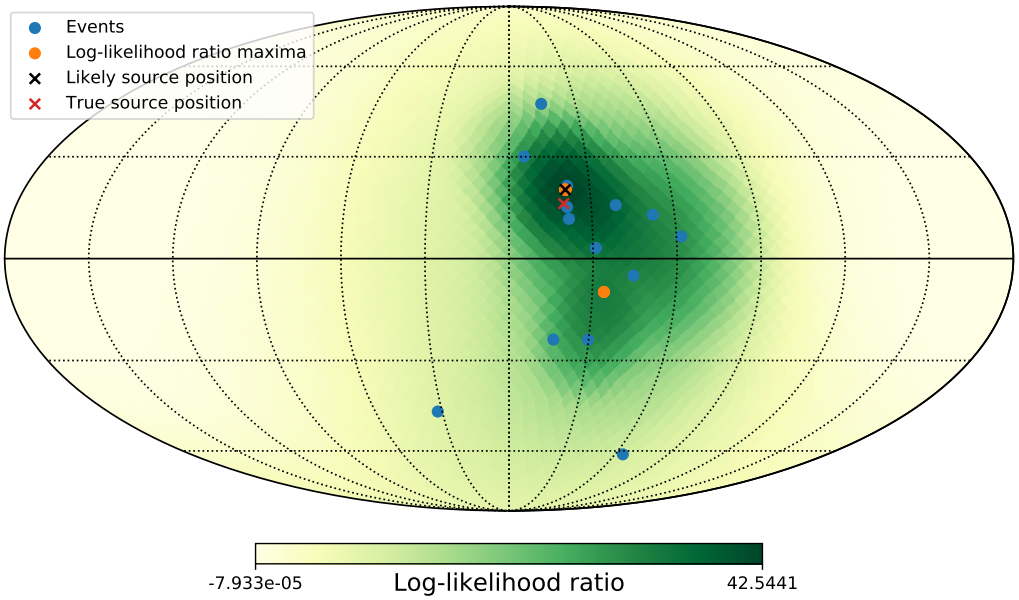

FIGURE 5.10: *Sky map showing the principle of spatial maximization. Maximization of the log-likelihood ratio is performed once for each event (blue points). In this example, two distinct maxima (orange points) are found and the largest is selected as the maxima of interest (indicated with the black cross). The color scale in the background shows the value of the log-likelihood ratio computed for each bin, which is for illustration purposes only and is not used in the analysis.*

angular resolution can potentially result in a large value of the log-likelihood ratio, but only a small value of n_s.

When maximizing the log-likelihood ratio, there may be multiple spatial maxima. To choose the one of highest interest for the analysis, the maximization is performed once for each event within the time window, while using the position of the given event as an initial guess of the position of the possible source. This ensures that all relevant maxima are found. The largest maxima with a value of n_s larger than the n_s-threshold is chosen. Requiring the maxima to pass the n_s-threshold prevents the analysis from choosing a maximum near a single isolated event with good angular resolution, as mentioned above. See Figure 5.10 for an example sky map.

5.4 Performance

In order to investigate the performance of the analysis, it should be tested on data containing simulated sources. This way, the data will contain a modeled source with a specific known strength that can be varied in order to estimate the *sensitivity* and *discovery potential*. When injecting a source, both its true position and its likely position found in the analysis are known, and the uncertainty on the source position can be estimated as the angular distance between them. The sensitivity and discovery potential is defined and presented in Section 5.4.2, and the uncertainty on the likely position on the source is shown in Section 5.4.1.

5.4.1 Uncertainty on source position

If a source is found in IceCube data, it will be informative to compare the result to other sources identified in for example gamma-rays or gravitational waves by other experiments. Therefore, the uncertainty on the potential source position is useful. Furthermore, it also helps reveal the performance of the analysis.

In order to examine the uncertainty on the source position, the angular spread between the true and the likely position of the source found by the analysis is estimated. This is repeated in a large number of scrambled trials, where each scrambled trial corresponds to performing the analysis on a year of scrambled data. In this estimate, only the time windows most likely to contain the signal are considered, i.e., the time window closest in time to the true time of the source that passes both the R_{KDE}-threshold and the threshold of 2 on the fitted value of n_s. Examples are shown in Figure 5.11. The angular spread is shown as a function of n_s. The left plot shows examples for two different average source energies 20 GeV and 100 GeV, with a fixed declination of 16 degrees.

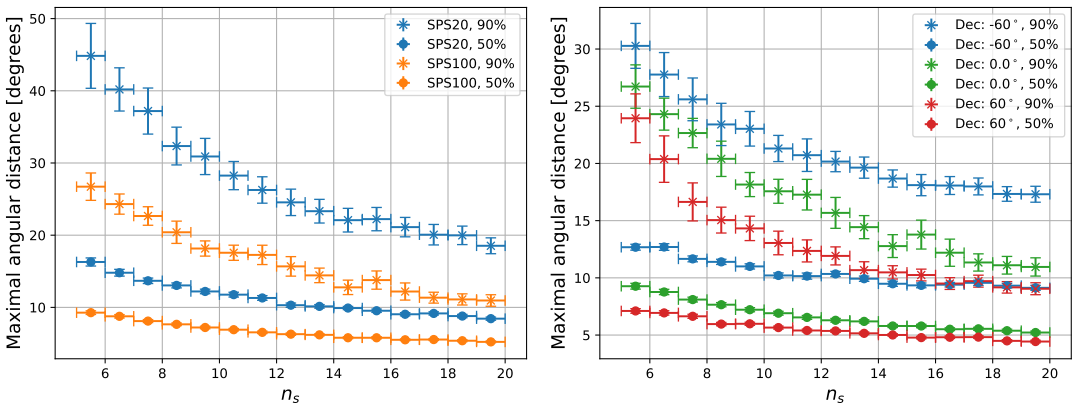

(A) (B)

FIGURE 5.11: *Angular spread between true and likely source positions. (a) Source declination is fixed at 16 degrees, results are shown for two different neutrino mean energies emitted from the source. (b) Average source energy is fixed at 100 GeV and results are shown for different source declinations.*

The right plot shows the angular spread for a few different source declinations, for a fixed SPS100 source energy spectrum. The percentages, 50% and 90%, refer to the confidence level, meaning that in 50 or 90 percent of the trials, the likely source position was found within the indicated angular distance of the true source position. The horizontal error bars indicate the size of the bins in n_s, while the vertical error bars specify the statistical uncertainty originating from the limited number of trials.

In general, the uncertainty on the source position decreases with the value of n_s because the true position can be estimated more accurately with a larger number of signal events. Additionally, the uncertainty decreases with energy as well as declination, which is caused by the better angular resolutions of higher energy events from larger declinations, see Figure 5.9 used for the angular resolution splines.

When reporting an observation of an astrophysical source, Figure 5.11 can be used to estimate the uncertainty on the given source. This is exemplified in Figure 5.12. The likely source position is indicated by the red cross around which two contours are drawn. The true position of the source is expected to be within the solid red contour with 50% probability and within the dashed contour with 90% probability.

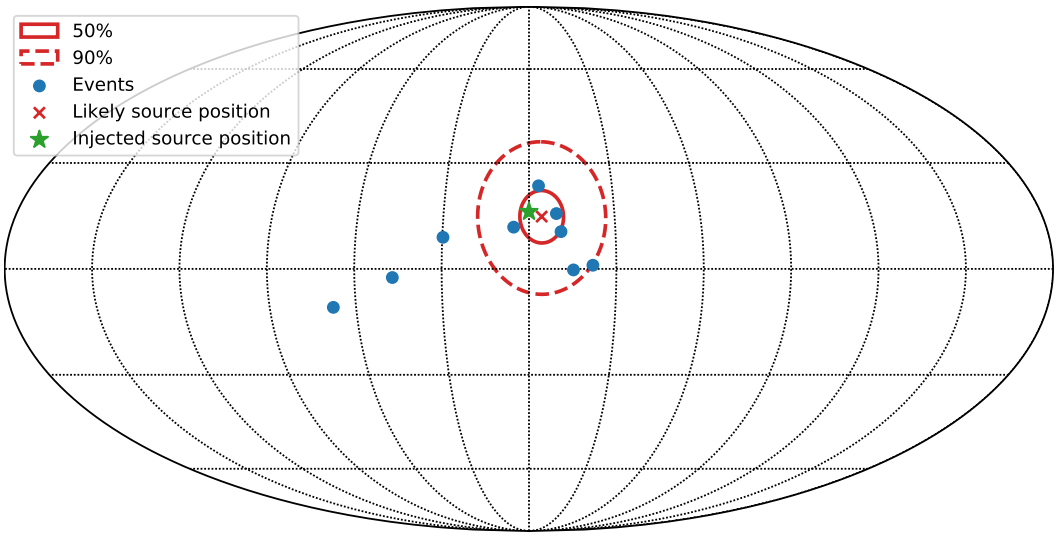

FIGURE 5.12: *Example of the uncertainty on the likely source position. The true position of the source (green star), is supposed to be within the solid red contour with 50% probability.*

5.4.2 Sensitivity and discovery potential

In order to estimate the sensitivity and discovery potential for the analysis, a *test statistic* is defined. The test statistic (TS) is a value that should be able to distinguish between the two possible hypotheses under examination, cf. Section 5.3.1, and it must be calculated in one specific way regardless of the existence of signal. In this work, the maximum of the maximized log-likelihood ratios is chosen. This means that for one year of scrambled data 100 time windows are considered on average, resulting in about 100 values of the maximized log-likelihood ratios. Subsequently, the test statistic is defined as the largest one, meaning that the test statistic is a single value for a whole year of data.

In the IceCube Collaboration the following definitions are standard and are used in this work:

> **Sensitivity** is estimated as the number of events/fluence required for 90% of the signal test statistic distribution to be larger than the median of the background distribution.
> **Discovery potential** is estimated as the number of events/fluence needed so that 50% of the signal test statistic distribution is larger than the test statistic value corresponding to the desired number of sigmas for the background distribution.

In this work, a 3σ discovery potential will be used. Figure 5.13 shows the background TS distribution together with an example of the signal TS distribution. The source strength is varied by varying the number of injected signal events until the requirements for the sensitivity and discovery potential are reached. For instance, a brighter source will result in an increased number of signal events. Stronger sources will affect the signal test statistic distribution by shifting it towards larger values.

In Figure 5.13a it is evident that the signal TS distribution is rather wide compared to the background TS distribution and both distributions have their peak at approximately the same position. This is an artifact from the Poisson distributed injection of events. In the specific example of the blue line with 7 signal events, the distribution is created by injecting a randomly drawn number of events (an integer) from a Poisson distribution with mean value 7.0. This is repeated in 5000 trials, where a year of scrambled data have been used in each. Consequently, some trials contain a small number of signal events, making those trials similar to trials containing background only. This causes the signal TS distribution to peak at the same position as the background TS distribution. Other trials contain a large number of signal events resulting in the long tail of the signal TS distribution. Furthermore, this explains that the peak of the signal distribution is more prominent for a lower number of signal events, while the tail becomes more dominating for larger numbers of signal events.

Figure 5.13b shows the same TS distribution created with 7 being the mean of the Poisson (blue distribution) compared to a TS distribution where the injected number of events is kept fixed. As expected, the distribution with the fixed signal is more narrow and peaks at a larger value.

Figure 5.14 shows the estimated sensitivity and discovery potential in terms of the number of signal events. Information about the energy of the source is not included directly in the calculation of the test statistic, but affects the results indirectly through the angular resolution that depends on the energy of the events. The resulting sensitivity and discovery potential for a source emitting higher energy neutrinos are better since the angular resolutions on average are better for higher energy events, cf. Figure 5.9. The sensitivity and discovery potential are better at low and high declinations due to the shape of the spline used for the background PDF $\mathcal{B}_i$, cf. Figure 5.8. Near equator (cos(zenith=0), a larger number of background events are expected, resulting in larger values of $\mathcal{B}_i$, which makes it necessary to observe more signal events in order to detect a source.

The sensitivities and discovery potentials in Figure 5.14 are given as the number of events needed in the final dataset in order to fulfill the requirements in the definitions of sensitivity and discovery potential. That is the number of

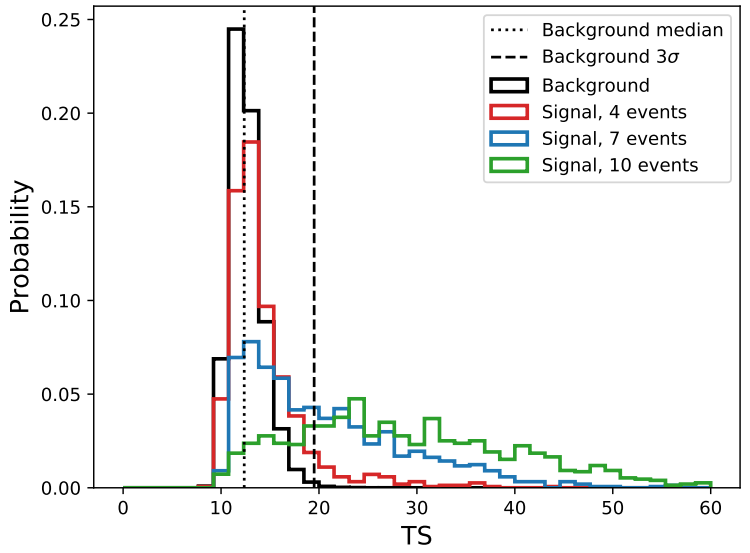

(A)

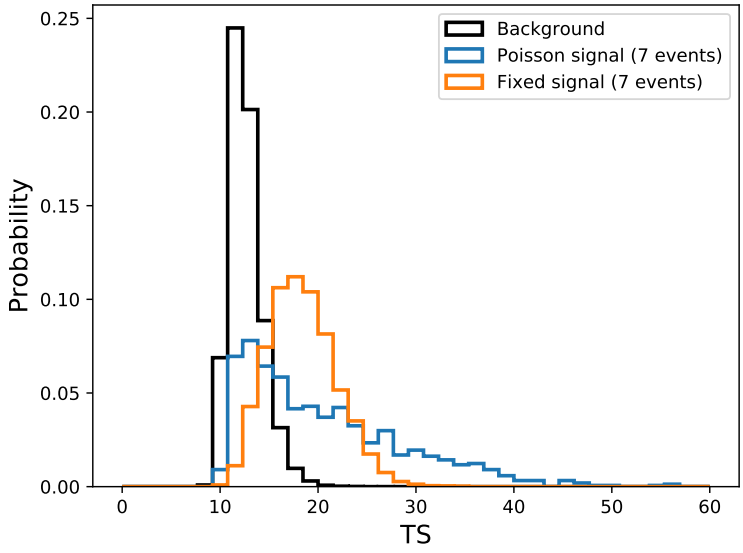

(B)

FIGURE 5.13: *Test statistic distributions for background based on 100000 trials and signal based on 5000 trials. The signal distributions are created using the SPS20 energy spectrum with a source injected at a declination of 16 degrees. (a) The sensitivity is reached for the number of injected signal events that results in 90% of the signal test statistic distribution being on the right-hand side of the dashed line, while the discovery potential is reached when the signal median overlaps with the dotted line. (b) Poisson distributed signal injection results in a wider signal TS distribution.*

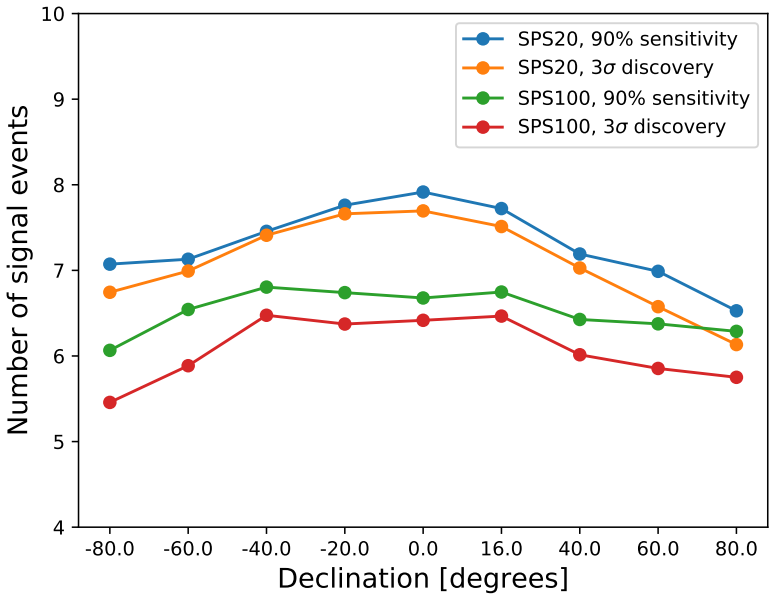

FIGURE 5.14: *The 90% sensitivity and 3σ discovery potential shown for neutrino sources with subphotospheric energy spectra with mean energies of 20 GeV and 100 GeV.*

events emitted from a source that are observed in the detector and pass all the cuts in the GRECO event selection. Hence, the number of signal events depends on the chosen event selection. In order to compare to specific astrophysical sources, the number of observed events must be converted into a fluence that is independent of the event selection. This is done by using the effective area for the analysis, cf. Figure 5.2, along with the expected energy spectrum of the source.

The number of observed events from an astrophysical source is given by

$$N = \int A_{eff}(E)\Phi(E)\mathrm{d}E, \tag{5.14}$$

with $A_{eff}(E)$ being the effective area and $\Phi(E)$ is the energy spectrum assumed for the source, i.e., the subphotospheric energy spectrum simplified as the Fermi-Dirac spectrum defined in Equation 5.1.

Consider Equation 5.1 written in the compact form

$$\Phi(E) = \mathcal{N} \cdot \Phi_0(E), \qquad \text{with} \qquad \Phi_0 = \frac{\left(\frac{E}{kT}\right)^2}{e^{\frac{E}{kT}} + 1}. \tag{5.15}$$

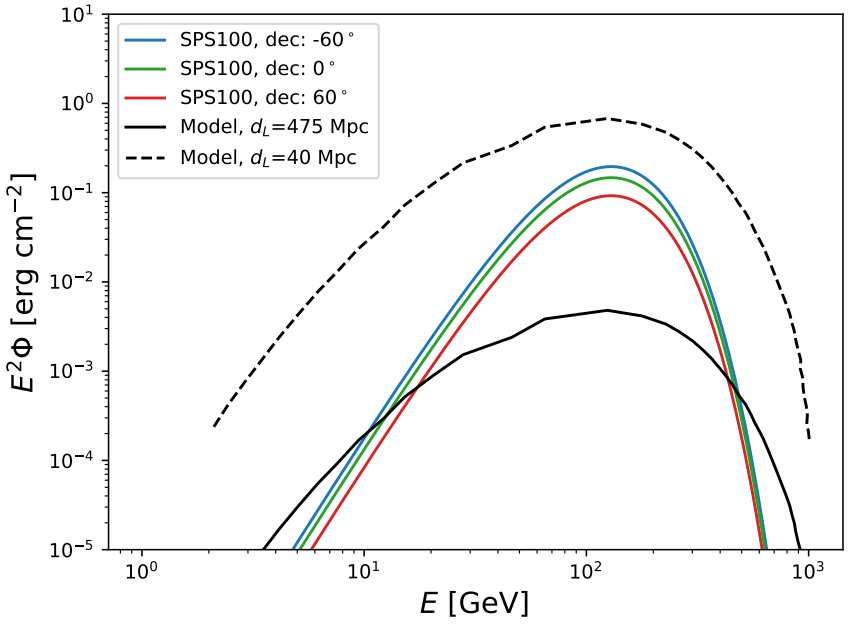

FIGURE 5.15: *The colored lines show three examples of the Fermi-Dirac fluence defined by Equation 5.1 and normalized to the value corresponding to the sensitivity in terms of number of signal events. The black solid line is the predicted model fluence from Ref. [23], see also Figure 4.1. The black dashed line is the same model but corresponds to a gamma-ray burst at a distance of ∼40 Mpc instead of ∼475 Mpc.*

Then an expression for the normalization factor $\mathcal{N}$ can be obtained by combining Equations 5.14 and 5.15

$$\mathcal{N} = \frac{N}{\int A_{eff}(E)\Phi_0(E)\mathrm{d}E}. \tag{5.16}$$

By using the number of signal events from Figure 5.14 as the parameter N, the normalization factor for the fluence is calculated using Equation 5.16, and subsequently the fluence is found using Equation 5.15. The estimated fluence is shown in Figure 5.15 for different declinations and is compared to the prediction (red thick curve from Figure 4.1 originally taken from Ref. [23]). The original prediction with a gamma-ray burst at a distance of approximately 475 Mpc is indicated by the solid black line. The dashed line corresponds to the same model rescaled to a distance of 40 Mpc, which is equivalent to the distance of the neutron star merger recently observed through both gravitational waves and gamma-rays, cf. Section 4.1. The fluence corresponding to the sensitivity for this analysis is below the predicted model fluence for a gamma-ray burst at

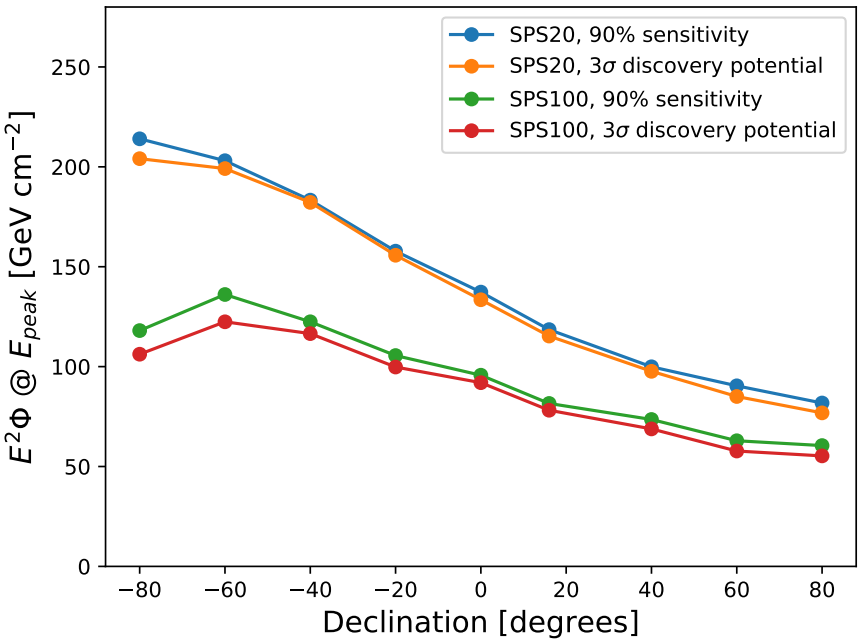

FIGURE 5.16: *Sensitivity and discovery potential in terms of fluence. Each point correspond to the peak fluence including those from Figure 5.15.*

a distance of 40 Mpc, and thus, the analysis developed in this work would be able to detect a gamma-ray burst following this specific model with the given strength/distance.

Each colored curve in Figure 5.15 corresponds to one point in Figure 5.14. The objective is to convert all points showing sensitivity and discovery potentials into a fluence. This is done by creating one fluence curve for each point, and then using the peak fluence as a reference point. The result is shown in Figure 5.16, where for instance, the second green point is equivalent to the peak of the blue curve in Figure 5.15.

The declination dependence shown in Figures 5.15 and 5.16 originates from the declination dependence of the effective area as shown in Figure 5.2. When the effective area is larger at the Northern Hemisphere, the required fluence emitted from an astrophysical source in order for the source to be observable in the dataset is smaller.

Throughout the analysis, both the time KDE bandwidth and the signal time distribution for the injected signal are set as 100 s. However, Figure 5.17 shows how the sensitivity in terms of the number of signal events depends on either of these parameters, while the other one is kept fixed at 100 s. Figure 5.17a, shows that the sensitivity is almost constant for signal emission time scales compara-

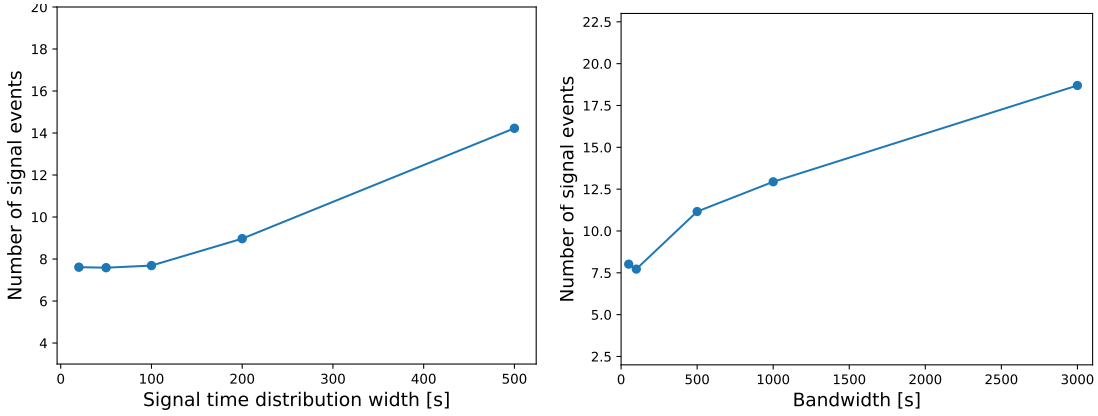

(A) (B)

FIGURE 5.17: *Sensitivity for the SPS20 energy spectrum at a declination of 16 degrees as a function of (a) the width of the signal time distribution and (b) the time KDE bandwidth.*

ble to or smaller than the bandwidth, and worsens if the signal emission times exceeds the bandwidth. This is reasonable, because a signal time distribution width larger than the bandwidth results in a smaller fraction of the signal neutrinos included in a time window. Hence, in order to include the same number of events in a single time window, the source must be stronger and thereby emit more neutrinos. Consequently, the bandwidth should ideally be equal to, or larger than, the expected signal emission time scales for the astrophysical sources. Figure 5.17b shows that the sensitivity worsens as the bandwidth increases. This results from the increasing number of expected background events within the time windows as they get larger. This means that, ideally, the bandwidth should be as small as possible. The conclusion from Figure 5.17 is that the bandwidth should be as small as possible, but never smaller than the expected signal emission time scale, meaning that the ideal bandwidth is the size of the signal time distribution.

5.4.3 Uncertainties

Since the fluctuations of the event rate in azimuth and time are averaged out, this is accounted for in the final results. This means that it should be examined how those fluctuations possibly affect the sensitivity/discovery potential. From Figure 5.3, the average fluctuation is estimated to be less than 15% in total. In order to be conservative, the discovery potentials are therefore found by increasing the total background data rate by 15%. Essentially, events are added

to the background sample by duplicating 15% randomly chosen events. The effect on the discovery potential is shown in Figure 5.18. From the ratio plot, it is evident that a 15% increase in the background rate results in an increase of less than 5% in the discovery potential.

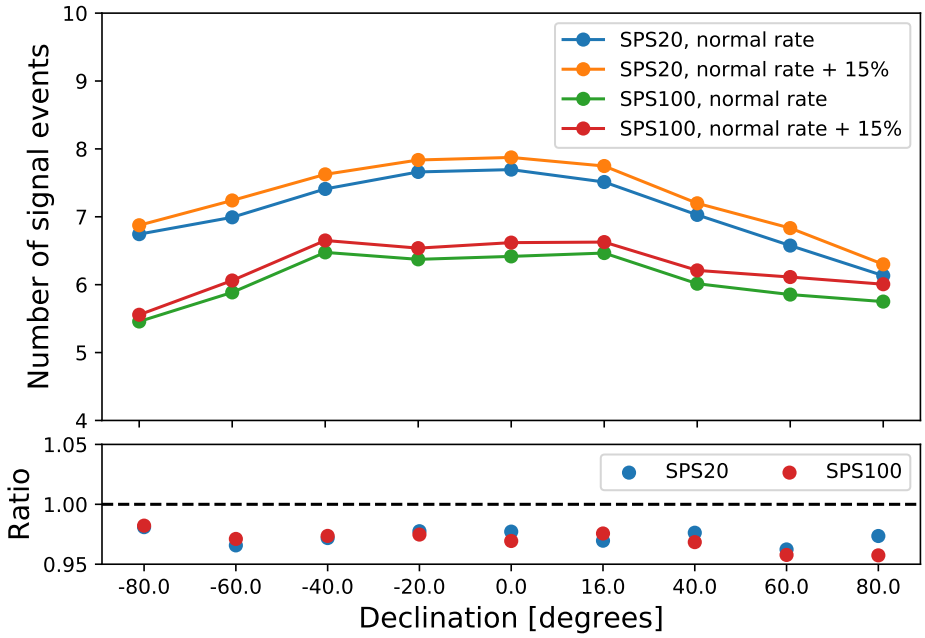

FIGURE 5.18: *Comparison between the discovery potential in terms of the number of signal events for the normal background rate and for an 15% increased background rate.*

5.4.4 Comparing to previous work

The analysis performed in this work is in many ways similar to the analysis described in Ref [21]. Both analyses strive to observe transient neutrino emission from astrophysical point sources by using data obtained with the IceCube-DeepCore detector. However, the analyses differ in multiple ways. For example, two different datasets are used, the previous analysis selected neutrinos from only the Northern Hemisphere, and includes only muon neutrinos resulting in tracks, while the analysis in this work is a full sky search using all flavors. Furthermore, the methods implemented are different. This analysis uses a KDE to preselect interesting time windows followed by a spatial maximum likelihood only on the selected events. The previous analysis performs the maximum likelihood analysis on all events and includes a time term in the likelihood instead.

The sensitivity from Ref. [21], both in terms of the number of events and the fluence, is listed in Table 5.1. It appears that the sensitivity in terms of the number of events is slightly better in the previous analysis, however, the sensitivity given in fluence is approximately a factor of 6 better in this work. This factor of 6 originates from the fact that both tracks and cascades from all neutrino flavors have been considered in this work, effectively resulting in a larger effective area for this analysis, especially at lower energies as seen in Figure 5.2.

TABLE 5.1: *Sensitivities from this and the previous analysis in terms of the number of signal events and the fluence.*

Parameter	This analysis	Previous analysis
Event sensitivity	$\sim$7.7	$\sim$5.5
Fluence sensitivity	$1.2{\cdot}10^{-3}\,\mathrm{GeV}^{-1}\,\mathrm{cm}^{-2}$	$0.7{\cdot}\,10^{-2}\,\mathrm{GeV}^{-1}\,\mathrm{cm}^{-2}$

5.5 Analysis design choices

Currently, the analysis functions as an offline search on already existing data. However, the prospect in the future is to implement it as a real-time search. Therefore, the analysis is designed and developed with the potential of running online.

The purpose of the time KDE is to locate multiplets of neutrino events in time, cf. 5.2. In a future online search, the KDE has an additional purpose. The positions of the events must be reconstructed in real-time in the online analysis before being used in the spatial maximum likelihood analysis, but doing so for

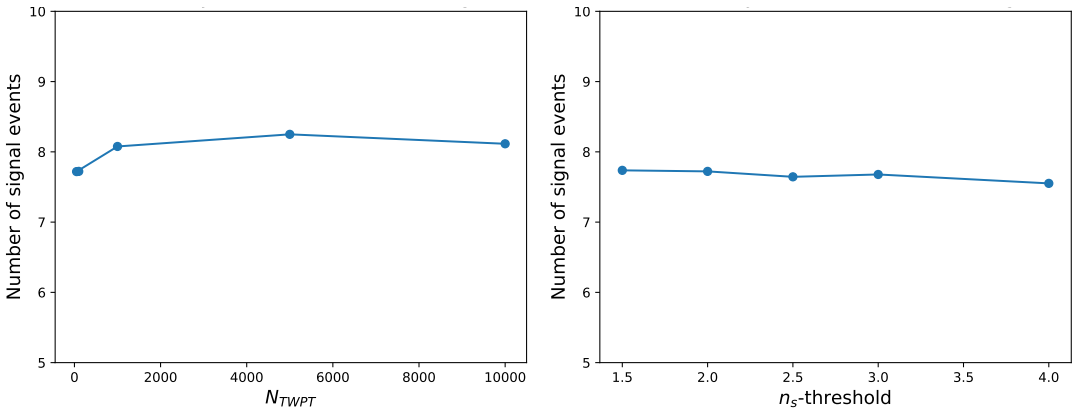

(A) (B)

FIGURE 5.19: *Sensitivity for the SPS20 energy spectrum with an injected source declination of 16 degrees as a function of (a) the parameter N_{TWPT} and (b) the threshold on n_s. In the former case, the average number of time windows are varied by effectively changing the R_{KDE}-threshold. The sensitivity is approximately constant in both cases.*

all events in the GRECO event selection is unfeasible. Therefore, the main purpose of the KDE is to preselect the neutrino events of interest based solely on their times, avoiding the need to reconstruct all events in real-time, and thereby improving the latency of the alert system. In this work, the R_{KDE}-threshold is chosen to give a N_{TWPT} of 100, and the threshold of 2 on the value of n_s is chosen to require a minimum of spatial clustering. In the framework of an online search, the threshold on the value of R_{KDE} can be set to a larger or smaller value, depending on the speed of the directional reconstruction and the desired latency of the alerts. Furthermore, the threshold on the value of n_s can be chosen to allow a given fraction of the time windows to pass. Each time window passing the n_s-threshold will result in the triggering of an alert. Effectively, this means that the n_s-threshold can be chosen to allow a desired number of alerts per year, depending on the wishes and possibilities from other collaborations, e.g., Fermi.

Although the two thresholds might be set differently in a real-time search, the sensitivity remains approximately constant. This result is shown in Figure 5.19 and is an artifact of the definition of the TS for the analysis and the existence of the time windows. The TS distribution for background, defined as the largest log-likelihood ratio for a year of scrambled data based on numerous trials, does not depend heavily on the thresholds. This is because the time windows are chosen to select the most promising times for transient emission. Therefore, the additional time windows found by decreasing R_{KDE} and

thereby increasing N_{TWPT} will predominantly result in smaller values of the log-likelihood ratio. If a relatively small value of the n_s-threshold is chosen, it will mainly cut away the smaller log-likelihood ratios, and hence this threshold will not affect the TS distribution and thereby the sensitivity heavily either. Naturally, if a very large value is chosen for either threshold, it will prevent the observation of any sources.

Chapter 6

Results from unblinding

The process of running the analysis on real data without scrambling the times is referred to as *unblinding*. In this way, the physics measurements of the analysis is obtained.

Section 6.1 contains the unblinding results, while Section 6.2 provides a discussion of the physics interpretation in the case of not observing any astrophysical sources with a neutrino emission exceeding the discovery potential presented in Section 5.4.2.

6.1 Unblinding results

The data is unblinded and the analysis is performed with the parameters fixed as specified in Table 6.1 as discussed in Chapter 5.

When running the analysis, 300 time KDE maxima are found above the R_{KDE}-threshold resulting in 300 time windows. After applying the threshold

TABLE 6.1: *Parameters used when performing the analysis. The time window width is defined as a factor of six larger than the time KDE bandwidth and the $R_{KDE}-$threshold is chosen based on the desired average number of expected time windows (N_{TWPT}) for three years of data.*

Parameter	Value
Time KDE bandwidth	100 s
Time window width	600 s
R_{KDE}-threshold	950.80
N_{TWPT} (for three years of data)	300
n_s-threshold	2

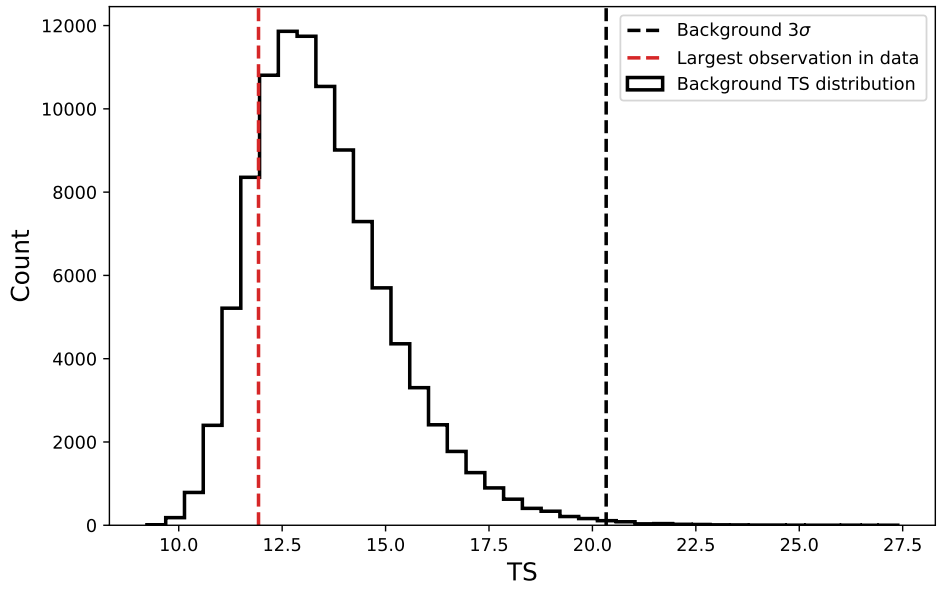

FIGURE 6.1: *Test statistic distribution for scrambled background plotted together with the 3σ value and the largest observation (log-likelihood ratio) found when performing the analysis on three years of GRECO data.*

TABLE 6.2: *Unblinding results.*

Variable	Value
Number of time windows found above KDE threshold	300
Number of time windows remaining after n_s-threshold	267
Largest observation (log-likelihood ratio)	11.93

on the value of n_s, 267 time windows remain. This means, that there were 267 relevant values of the log-likelihood ratio corresponding to a possible neutrino source. The largest of these are compared to the 3σ value for the background test statistic distribution based on scrambled trials. The result can be seen in Figure 6.1. The 3σ TS value for scrambled background is 20.33, while the largest observation in the data yields a log-likelihood ratio of 11.93. Since the largest log-likelihood ratio is smaller than the 3σ TS for background, there is no evidence of transient low-energy neutrino emission from point sources in these three years of data. Table 6.2 shows the unblinding results.

6.2 Volumetric rate limit

Given the non-observation of transient neutrino point sources, it is possible to constrain the volumetric rate of transient sources based on the discovery potential shown in Section 5.4.2. The volumetric rate is denoted $\dot{\rho}$ and is a measure of the rate at which the transient astrophysical phenomena under consideration happen per unit volume in the local universe. In this work, that corresponds to a limit on the rate of gamma-ray bursts given the assumed subphotospheric model. In practice, a region in the parameter space of volumetric rate versus bolometric energy $\mathcal{E}$ of the neutrinos is excluded. The bolometric energy corresponds to the total neutrino energy emitted from the source.

The peak fluence defining the discovery potential is found by following Ref. [37]

$$E^2\Phi_\nu = \int_0^\infty \mathrm{d}z \frac{\mathcal{E}}{4\pi d_L^2(z)} \frac{\mathrm{d}N}{\mathrm{d}z} e^{-N(z)}, \tag{6.1}$$

where the factor

$$\frac{\mathrm{d}N}{\mathrm{d}z} e^{-N(z)},$$

describes the probability of the closest transient neutrino source being at the redshift z. The parameter N is a measure of the expected number of sources within redshift z and is given by

$$N(z) = \dot{\rho} T f_{sky} \frac{4\pi}{3} d_c^3(z), \tag{6.2}$$

where T is the livetime of the analysis, meaning the detector runtime for the used dataset, and f_{sky} is the fraction of the sky considered. Since this work is a full sky search $f_{sky} = 1$.

The luminosity distance d_L of the source is related to its comoving distance through

$$d_L(z) = (1+z) d_c(z). \tag{6.3}$$

The comoving distance $d_c(z)$ takes the expansion of the universe into account and therefore does not change with time. It is written as

$$d_c(z) = \int_0^z \frac{c}{H(z')} \mathrm{d}z', \tag{6.4}$$

with c being the speed of light and $H(z)$ is the Hubble parameter. Assuming a matter and dark energy dominated universe without curvature, the Hubble parameter takes the form [38]

$$H(z)^2 = H_0^2 \left((1+z)^3 \Omega_m + \Omega_\Lambda \right), \tag{6.5}$$

where the Hubble constant H_0 is the value of the Hubble parameter at the present time. In this work, the value $70.03 \pm 1.42\,\mathrm{km\,s^{-1}\,Mpc^{-1}}$, recently reported by the Hubble Space Telescope, is adopted [39].
The density parameters for matter and dark energy are assumed to be $\Omega_m = 0.3$ and $\Omega_\Lambda = 0.7$, respectively [40].

The probability distribution of the closest source with respect to redshift is then found by combining Equations 6.2 and 6.4 and differentiating with respect to the redshift, which result in

$$\frac{\mathrm{d}N}{\mathrm{d}z} = \dot{\rho} T 4\pi \frac{c}{H(z)} d_c^2. \tag{6.6}$$

Substituting Equations 6.3 and 6.6 into Equation 6.1 yields

$$\begin{aligned} E^2\Phi_\nu &= \int_0^\infty \mathrm{d}z \frac{\mathcal{E}}{4\pi(1+z)^2 d_c^2(z)} \dot{\rho} T 4\pi \frac{c}{H(z)} d_c^2(z), \\ &= \dot{\rho} T c \mathcal{E} \int_0^\infty \mathrm{d}z \frac{1}{(1+z)^2 H(z)} e^{-N(z)}. \end{aligned} \tag{6.7}$$

By combining Equations 6.2, 6.4 and 6.7 we obtain the final expression

$$E^2\Phi_\nu = \dot{\rho} T c \mathcal{E} \int_0^\infty \mathrm{d}z \frac{1}{(1+z)^2 H(z)} e^{-\dot{\rho} T \frac{4\pi}{3} (\int_0^z \frac{c}{H(z')} \mathrm{d}z')^3}. \tag{6.8}$$

From Equation 6.8 correlated values of $\dot{\rho}$ and $\mathcal{E}$ are found. As mentioned, $E^2\Phi_\nu$ corresponds to the peak fluence defining the discovery potential. However, the discovery potential in this analysis is not just a single number but rather a function of declination for each neutrino mean energy of the source, cf. Figure 5.16.

The constraints on the volumetric rate of transient sources are shown in Figure 6.2. This is constructed from the discovery potentials based on the increased background rate, which ensures that uncertainties due to fluctuations are accounted for, cf. Section 5.4.3. Additionally, separate plots showing the constraints on the volumetric rate are made for each mean neutrino energy for the source considered in this work (20 GeV and 100 GeV), with the declination dependence of the discovery potential indicated by light blue bands.

The stars in Figure 6.2 are plotted for comparison and correspond to models for low and high energy gamma-ray bursts [23, 41]. The bolometric neutrino energies of gamma-ray bursts are not well-known and therefore, for simplicity, they are assumed to be equal to the associated gamma-ray energies. The total neutrino and gamma-ray energy is expected to be of the same order of magnitude, considering only neutrinos and gamma-rays emitted via decay of pions created through hadronuclear interactions, as explained in Section 4.2.

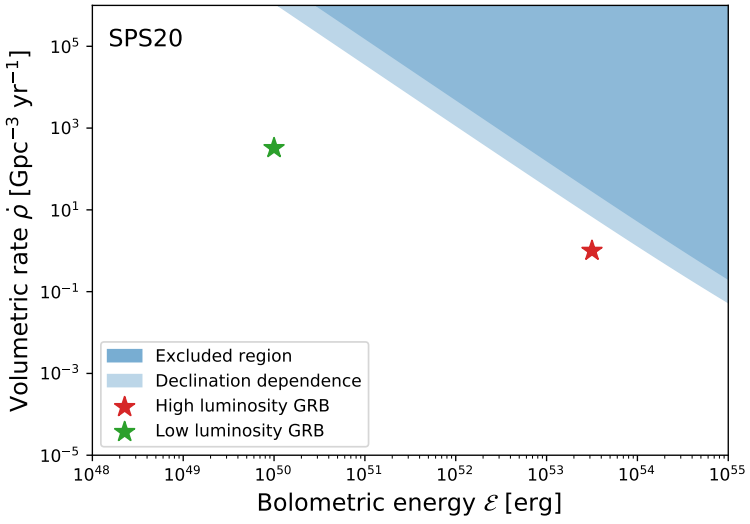

(A)

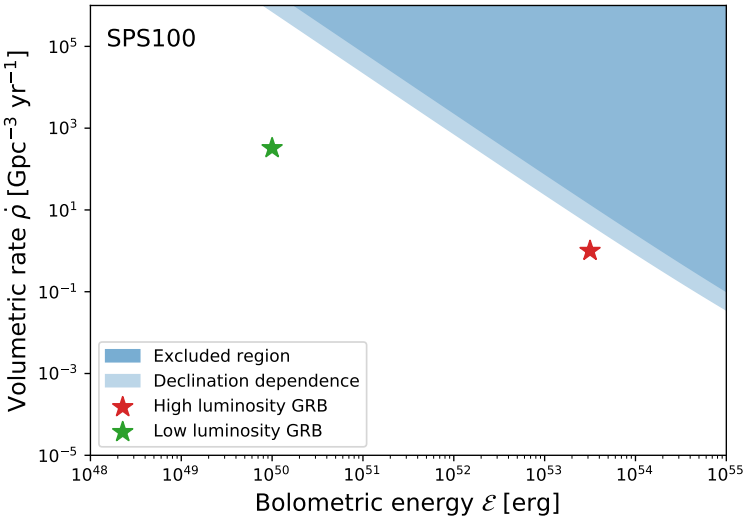

(B)

FIGURE 6.2: *The 3σ excluded region in the volumetric rate and bolometric energy parameter space for the astrophysical transient sources following a subphotospheric energy spectrum with mean energy (a) 20 GeV and (b) 100 GeV. The light blue bands indicate the declination dependence of the discovery potential. Approximated predictions for low and high luminosity gamma-ray bursts are plotted on top for comparison.*

Chapter 7

Conclusion and outlook

In this work, an analysis with the purpose of finding neutrinos originating from astrophysical transient point sources has been developed. After having it reviewed and approved by the IceCube Collaboration it has been performed on data collected with the IceCube detector including the low-energy extension DeepCore. The focus has been on low-energy neutrinos in the sub-TeV range, and more specifically three years of data from the GRECO sample have been used.

Sensitivities and discovery potentials assuming gamma-ray bursts emitting neutrinos following subphotospheric energy spectra have been estimated and it has been shown that the analysis is sensitive to high luminosity gamma-ray bursts.

It is concluded that this analysis found no evidence of transient neutrino emission originating from generic point sources present in the data. Upper limits constraining the volumetric rate of transient sources in the local universe have been presented.

This analysis is also the foundation of a future real-time alert system. The reason for the time KDE and the associated time windows is to have a preselection of the interesting neutrino events. This is important in the case of a real-time search, because the reconstruction of the directional information about the events is extremely time consuming. By using the time windows as a preselection, the likelihood method is only performed on a smaller subset of the events. Therefore, the reconstruction is unnecessary for the majority of the events since the directional information is only included in the likelihood and not in the KDE.

By running the analysis real-time (online) instead of on already existing archived data, evidence of transient neutrino emission from point sources can be found continuously. Subsequently, alerts can be published and other exper-

iments (Fermi, LIGO, etc.) can search for correlations with their own data. In this respect, a future alert system based on this analysis can contribute to the multimessenger astronomy.

With the next generation of the IceCube Neutrino Observatory, *IceCube-Gen2*, the collaboration seeks to expand the volume of the instrumented ice to a total of 10 km^3. The additional volume will be less densely instrumented with 120 new strings, with the purpose of increasing the effective area, especially for high energy neutrinos. Furthermore, several new strings will be deployed within the already existing low-energy extension DeepCore, resulting in better sensitivity at lower energies.

The DOMs used for IceCube-Gen2 will include different types with the PMTs pointing in multiple directions. This will further increase the angular resolutions for some events, especially events originating from the Southern Sky.

Effectively, IceCube-Gen2 will lead to improved low-energy point source searches by providing the potential of observing a larger number of astrophysical low-energy events with better angular accuracy.

Bibliography

[1] C. L. Cowan, F. Reines, F. B. Harrison, H. W. Kruse, and A. D. McGuire. Detection of the free neutrino: A Confirmation. *Science*, 124:103–104, 1956.

[2] C. L. Cowan, F. Reines, F. B. Harrison, H. W. Kruse, and A. D. McGuire. Detection of the free neutrino: A Confirmation. *Science*, 124:103–104, 1956.

[3] Standard Model `https://www.physik.uzh.ch/en/researcharea/lhcb/outreach/StandardModel.html` (Last visited: Aug. 20, 2019).

[4] Raymond Davis, Don S. Harmer, and Kenneth C. Hoffman. Search for neutrinos from the sun. *Phys. Rev. Lett.*, 20:1205–1209, May 1968.

[5] John N. Bahcall. Solar Neutrinos. I. Theoretical. *Phys. Rev. Lett.*, 12:300–302, Mar 1964.

[6] R.L. Helmer. First results from the sudbury neutrino observatory. *Nuclear Physics B - Proceedings Supplements*, 111(1):122 – 127, 2002.

[7] B. Pontecorvo. Inverse beta processes and nonconservation of lepton charge. *Sov. Phys. JETP*, 7:172–173, 1958. [Zh. Eksp. Teor. Fiz.34,247(1957)].

[8] Ziro Maki, Masami Nakagawa, and Shoichi Sakata. Remarks on the unified model of elementary particles. *Prog. Theor. Phys.*, 28:870–880, 1962.

[9] Ivan Esteban, M. C. Gonzalez-Garcia, Michele Maltoni, Ivan Martinez-Soler, and Thomas Schwetz. Updated fit to three neutrino mixing: exploring the accelerator-reactor complementarity. *JHEP*, 01:087, 2017.

[10] R. Abbasi et al. The Design and Performance of IceCube DeepCore. *Astropart. Phys.*, 35:615–624, 2012.

[11] M. G. Aartsen et al. The IceCube Neutrino Observatory: Instrumentation and Online Systems. *JINST*, 12(03):P03012, 2017.

[12] J. A. Formaggio and G. P. Zeller. From eV to EeV: Neutrino Cross Sections Across Energy Scales. *Rev. Mod. Phys.*, 84:1307–1341, 2012.

[13] I. M. Frank and I. E. Tamm. Coherent visible radiation of fast electrons passing through matter. *Compt. Rend. Acad. Sci. URSS*, 14(3):109–114, 1937. [Usp. Fiz. Nauk93,no.2,388(1967)].

[14] P. A. Čerenkov. Visible radiation produced by electrons moving in a medium with velocities exceeding that of light. *Phys. Rev.*, 52:378–379, Aug 1937.

[15] Morten Medici. Search for Dark Matter Annihilation in the Galactic Halo using IceCube. PhD thesis, 2017.

[16] David Freiherr Heereman von Zuydtwyck. HitSpooling: An Improvement for the Supernova Neutrino Detection System in IceCube, phd thesis, 2015.

[17] B. P. Abbott et al. Observation of Gravitational Waves from a Binary Black Hole Merger. *Phys. Rev. Lett.*, 116(6):061102, 2016.

[18] B. P. Abbott et al. Multi-messenger Observations of a Binary Neutron Star Merger. *Astrophys. J.*, 848(2):L12, 2017.

[19] John F. Beacom. The Diffuse Supernova Neutrino Background. *Ann. Rev. Nucl. Part. Sci.*, 60:439–462, 2010.

[20] P. Padovani, P. Giommi, E. Resconi, T. Glauch, B. Arsioli, N. Sahakyan, and M. Huber. Dissecting the region around IceCube-170922A: the blazar TXS 0506+056 as the first cosmic neutrino source. *Mon. Not. Roy. Astron. Soc.*, 480(1):192–203, 2018.

[21] M. G. Aartsen et al. Search for Transient Astrophysical Neutrino Emission with IceCube-DeepCore. *Astrophys. J.*, 816(2):75, 2016.

[22] M. J. Rees and P. Mészáros. Relativistic fireballs: energy conversion and time-scales. *Monthly Notices of the Royal Astronomical Society*, 258(1):41P–43P, 09 1992.

[23] Kohta Murase, Kazumi Kashiyama, and Peter Mészáros. Subphotospheric Neutrinos from Gamma-Ray Bursts: The Role of Neutrons. *Phys. Rev. Lett.*, 111:131102, 2013.

[24] Soebur Razzaque, Peter Mészáros, and Eli Waxman. Tev neutrinos from core collapse supernovae and hypernovae. *Phys. Rev. Lett.*, 93:181101, Oct 2004.

[25] Luis A. Anchordoqui et al. Cosmic Neutrino Pevatrons: A Brand New Pathway to Astronomy, Astrophysics, and Particle Physics. *JHEAp*, 1-2:1–30, 2014.

[26] M. G. Aartsen et al. A combined maximum-likelihood analysis of the high-energy astrophysical neutrino flux measured with IceCube. *Astrophys. J.*, 809(1):98, 2015.

[27] Victor Hess. On the Observations of the Penetrating Radiation during Seven Balloon Flights. 2018.

[28] C. Patrignani et al. (Particle Data Group). Review of particle physics. *Chinese Physics C*, 40(10):100001, oct 2016.

[29] Takaaki Kajita. Atmospheric neutrinos. *Advances in High Energy Physics*, 2012.

[30] P. Desiati, T. Kuwabara, T. K. Gaisser, S. Tilav, and D. Rocco. Seasonal Variations of High Energy Cosmic Ray Muons Observed by the IceCube Observatory as a Probe of Kaon/Pion Ratio. In *Proceedings, 32nd International Cosmic Ray Conference (ICRC 2011): Beijing, China, August 11-18, 2011*, volume 1, pages 78–81, 2011.

[31] Yu Seon Jeong, Atri Bhattacharya, Rikard Enberg, C. S. Kim, Mary Hall Reno, Ina Sarcevic, and Anna Stasto. Prompt atmospheric neutrino flux. *PoS*, ICHEP2016:083, 2016.

[32] M. G. Aartsen et al. Measurement of the Atmospheric ν_e Spectrum with IceCube. *Phys. Rev.*, D91:122004, 2015.

[33] M. G. Aartsen et al. Measurement of Atmospheric Tau Neutrino Appearance with IceCube DeepCore. *Phys. Rev.*, D99(3):032007, 2019.

[34] M. G. Aartsen et al. Search for Prompt Neutrino Emission from Gamma-Ray Bursts with IceCube. *Astrophys. J.*, 805(1):L5, 2015.

[35] John T. Kent. The fisher-bingham distribution on the sphere. *Journal of the Royal Statistical Society. Series B (Methodological)*, 44(1):71–80, 1982.

[36] Morihiro Honda, T. Kajita, K. Kasahara, and S. Midorikawa. A New calculation of the atmospheric neutrino flux in a 3-dimensional scheme. *Phys. Rev.*, D70:043008, 2004.

[37] Markus Ahlers and Francis Halzen. Opening a New Window onto the Universe with IceCube. *Prog. Part. Nucl. Phys.*, 102:73–88, 2018.

[38] David W. Hogg. Distance measures in cosmology. 1999.

[39] Adam G. Riess, Stefano Casertano, Wenlong Yuan, Lucas M. Macri, and Dan Scolnic. Large Magellanic Cloud Cepheid Standards Provide a 1% Foundation for the Determination of the Hubble Constant and Stronger Evidence for Physics Beyond LambdaCDM. *Astrophys. J.*, 876(1):85, 2019.

[40] P. A. R. Ade et al. Planck 2015 results. XIII. Cosmological parameters. *Astron. Astrophys.*, 594:A13, 2016.

[41] Enwei Liang, Bing Zhang, and Z. G. Dai. Low Luminosity Gamma-Ray Bursts as a Unique Population: Luminosity Function, Local Rate, and Beaming Factor. *Astrophys. J.*, 662:1111–1118, 2007.

[42] Mark Thomson. *Modern particle physics*. Cambridge University Press, New York, 2013.

Appendix A

Neutrino oscillation — a two flavor model

As mentioned, neutrinos exist in three different flavors corresponding to the charged leptons. However, for simplicity, we will start by considering only two different flavor states (weak eigenstates) ν_α and ν_β. In this simplified example neutrinos have two different mass eigenstates as well, namely ν_1 and ν_2. It is the mass eigenstates that correspond to the physical states, i.e., the solutions to the wave equation describing the particles. The flavor and mass states are related through the *mixing angle* θ by [42]

$$\begin{bmatrix} \nu_\alpha \\ \nu_\beta \end{bmatrix} = \begin{bmatrix} \cos(\theta) & \sin(\theta) \\ -\sin(\theta) & \cos(\theta) \end{bmatrix} \begin{bmatrix} \nu_1 \\ \nu_2 \end{bmatrix}, \tag{A.1}$$

Effectively, the matrix in Equation A.1 is equivalent to a two-dimensional rotation matrix, meaning that the flavor states are similar to the mass states rotated around the origin with an angle of θ.

Using the bra-ket notation Equation A.1 can be rewritten as

$$|\nu_\alpha\rangle = \cos(\theta)\,|\nu_1\rangle + \sin(\theta)\,|\nu_2\rangle\,, \qquad |\nu_\beta\rangle = -\sin(\theta)\,|\nu_1\rangle + \cos(\theta)\,|\nu_2\rangle\,.$$

This is the time independent case, where the states are stationary states. The flavor states are quantum mechanical, coherent, linear, superpositions of the mass eigenstates. A mixing angle different from zero results in *neutrino mixing*.

Suppose a neutrino of flavor state ν_α is created at time $t = 0$. Then in order to find the time evolution of the flavor state, each mass eigenstate is multiplied by the phase factor

$$e^{-iE_j t},$$

where the subscript $j = 1, 2$ denotes the index of the mass state. This is in

natural units, which will be used throughout this whole chapter. This yields

$$|\nu_\alpha(t)\rangle = \cos(\theta)\,|\nu_1\rangle\, e^{-iE_1 t} + \sin(\theta)\,|\nu_2\rangle\, e^{-iE_2 t}. \tag{A.2}$$

A generic expression for the probability of the neutrino having transitioned into a state $|\nu_\beta\rangle$ from another state $|\nu_\alpha\rangle$ at time t is given by the squared amplitudes/inner products

$$P_{\nu_\alpha \to \nu_\beta} = |\langle \nu_\beta | \nu_\alpha(t)\rangle|^2 \tag{A.3}$$

Combining Equations A.2 and A.3 we obtain

$$\begin{aligned} P_{\nu_\alpha \to \nu_\beta} &= |\langle \nu_\beta | \nu_\alpha(t)\rangle|^2 \\ &= \left|(-\sin(\theta)\,\langle \nu_1| + \cos(\theta)\,\langle \nu_2|) \cdot \left(\cos(\theta)e^{-iE_1 t}\,|\nu_1\rangle + \sin(\theta)e^{-iE_2 t}\,|\nu_2\rangle\right)\right|^2 \\ &= \left|-\sin(\theta)\cos(\theta)e^{-iE_1 t}\,\langle \nu_1|\nu_1\rangle - \sin^2(\theta)e^{-iE_2 t}\,\langle \nu_1|\nu_2\rangle \right. \\ &\quad \left. + \cos^2(\theta)e^{-iE_1 t}\,\langle \nu_2|\nu_1\rangle + \cos(\theta)\sin(\theta)e^{-iE_2 t}\,\langle \nu_2|\nu_2\rangle\right|^2. \end{aligned} \tag{A.4}$$

Since the physical mass states spans an orthonormal basis the scalar/inner products between them must obey

$$\langle \nu_i | \nu_j \rangle = \delta_{ij},$$

where δ_{ij} is the Kronecker delta function. Using this, Equation A.4 can be rewritten

$$\begin{aligned} P_{\nu_\alpha \to \nu_\beta} &= \left|-\sin(\theta)\cos(\theta)e^{-iE_1 t} + \sin(\theta)\cos(\theta)e^{-iE_2 t}\right|^2 \\ &= \left|\sin(\theta)\cos(\theta)(e^{-iE_2 t} - e^{-iE_1 t})\right|^2 \\ &= \sin^2(\theta)\cos^2(\theta)\left|e^{-iE_2 t} - e^{-iE_1 t}\right|^2. \end{aligned} \tag{A.5}$$

The squared absolute value is expanded using the complex conjugate and in order to rewrite the sine and cosine factors we use the rule

$$\sin(\theta)\cos(\theta) = \frac{1}{2}\sin(2\theta).$$

For Equation A.5 this yields

$$\begin{aligned} P_{\nu_\alpha \to \nu_\beta} &= \frac{1}{4}\sin^2(2\theta)\left(e^{-iE_2 t} - e^{-iE_1 t}\right)\left(e^{iE_2 t} - e^{iE_1 t}\right) \\ &= \frac{1}{4}\sin^2(2\theta)\left(2 - e^{i(E_2 - E_1)t} - e^{-i(E_2 - E_1)t}\right) \\ &= \frac{1}{2}\sin^2(2\theta)\left(1 - \frac{e^{i(E_2 - E_1)t} + e^{-i(E_2 - E_1)t}}{2}\right) \end{aligned} \tag{A.6}$$

Using the following two trigonometric rules

$$\cos(\phi) = \frac{e^{i\phi} + e^{-i\phi}}{2} \qquad \text{and} \qquad \sin^2\left(\frac{\phi}{2}\right) = \frac{1}{2} - \frac{\cos(\phi)}{2},$$

we get

$$\begin{aligned} P_{\nu_\alpha \to \nu_\beta} &= \sin^2(2\theta)\left(\frac{1}{2} - \frac{1}{2}\cos((E_2 - E_1)t)\right) \\ &= \sin^2(2\theta)\sin^2\left(\frac{(E_2 - E_1)t}{2}\right). \end{aligned} \tag{A.7}$$

This is the expression for the transition probability of the neutrino as a function of the energy difference of the mass eigenstates. The energies are related to the mass of the states through Einsteins mass-energy equivalence

$$E^2 = m^2 + p^2 \Rightarrow E = \sqrt{m^2 + p^2} = (m^2 + p^2)^{\frac{1}{2}}. \tag{A.8}$$

Using the binomial formula

$$(x+y)^n = \sum_{k=0}^{n} \binom{n}{k} x^{n-k} y^k \qquad \text{with} \qquad \binom{n}{k} = \frac{n!}{k!(n-k)!},$$

the energy from Equation A.8 can be approximated by

$$E = p + \frac{m^2}{2p} - \frac{m^4}{4p^3} + ... \simeq p + \frac{m^2}{2p}. \tag{A.9}$$

All terms except for the first two are negligible and have been omitted. Equation A.9 is substituted into Equation A.7, and we finally acquire

$$\begin{aligned} P_{\nu_\alpha \to \nu_\beta} &= \sin^2(2\theta)\sin^2\left(\frac{\left(p + \frac{m_2^2}{2p} - p + \frac{m_1^2}{2p}\right)t}{2}\right) \\ &= \sin^2(2\theta)\sin^2\left(\frac{(m_2^2 - m_1^2)t}{4p}\right) \\ &= \sin^2(2\theta)\sin^2\left(\frac{(m_2^2 - m_1^2)t}{4E}\right). \end{aligned} \tag{A.10}$$

In the last equality the neutrino is assumed to be relativistic and therefore, $p \approx E$. This shows that if the mass eigenstates of the neutrinos are different the particles will *oscillate* between the flavor states as they travel through time.

This result is able to fully account for the deficit of the solar electron neutrinos — they simply oscillate into other flavors during their travel from the Sun towards Earth.

Since neutrinos only oscillate if their mass states are different, this implies that neutrinos are not massless as described by the Standard Model. Hence, this is one of the deficiencies of the Standard Model.